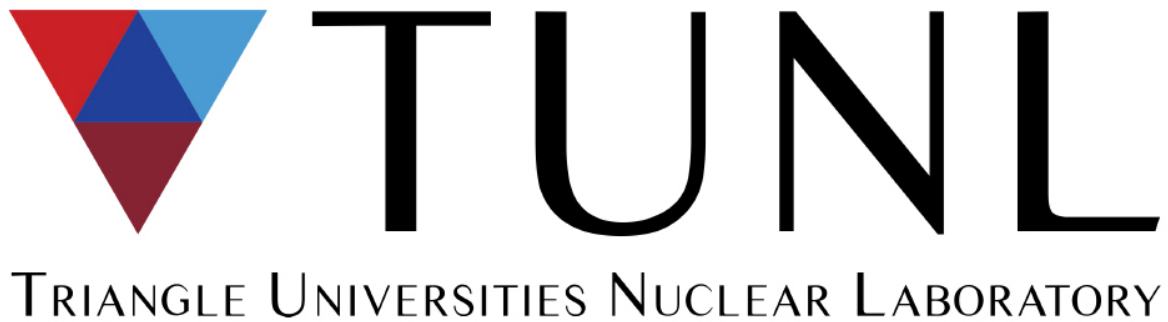


TUNL REU V

RESEARCH REPORT

19 MAY 2019 – 27 JULY 2019



Duke University
North Carolina Central University
North Carolina State University
University of North Carolina at Chapel Hill

Box 90308, Durham, North Carolina 27708-0308, USA

The research described in this report is supported by the United States Department of Energy, Office of Science, under:

Grant No. DE-SC0010007 (Duke University High-Energy Physics Group),
Grant No. DE-FG02-97ER41033 (Duke University/TUNL),
Grant No. DE-FG02-97ER41042 (North Carolina State University), and
Grant No. DE-FG02-97ER41041 (University of North Carolina).

The TUNL Research Experiences for Undergraduates (REU) Program is supported by the National Science Foundation under:

Grant No. NSF-PHY-1757783.

Contents

Introduction	iv
Personnel	v
1 Research Based at Duke	1
1.1 Finding a Material with a Low Energy Threshold for Charged-Current Neutrino Interactions	2
1.2 Sensitivity Study to Identify Important Nuclear Reactions in X-Ray Burst Nucleosynthesis	4
1.3 Evaluating the Possibility of Reconstructing Polarized Λ^0 Hyperons in CLAS12 at Jefferson Lab	6
1.4 Measurements of $^{124}\text{Sn}(\gamma, n)$ and $^{169}\text{Tm}(\gamma, n)$ Cross Sections at 13 MeV	9
1.5 Scrubbing System Supporting Tritium Gas Target for Research at HI γ S	12
1.6 Preparations for Compton Scattering from Cryogenic Liquid ^3He at HI γ S	15
1.7 Earth's Field Nuclear Magnetic Resonance	17
1.8 Development of Pelletron Accelerator for High Precision Calibration of Silicon Detectors	20
2 Research Based at CERN	23
2.1 Studies of Top Quark Decay Kinematics	24
2.2 Tagging $c\bar{c}$ Events via Hadronic Decay Modes of J/ψ at ATLAS	27
2.3 Photo-bombing the Trigger: A Study of the Potential of Pileup in ATLAS Analysis	29
2.4 Estimating the Background of Dark-QCD Processes	32

Introduction

An important national goal is to develop a diverse, internationally competitive, and globally engaged workforce in science and engineering. The Research Experiences for Undergraduates (REU) program is part of the effort to achieve that goal. The REU program at the Triangle Universities Nuclear Laboratory (TUNL) and Duke University provides a ten-week opportunity for undergraduate students to pursue research in the areas of nuclear and particle physics. This allows promising physics majors to broaden their education through participation in research at the frontiers of these exciting scientific fields.

In 2019, thirteen students participated in the TUNL REU Program: nine spent the summer working on nuclear physics projects on the Duke campus, while the other four spent four weeks at Duke and six weeks at the European Center for Nuclear Research (CERN) near Geneva, Switzerland, working on particle physics projects. Having the nuclear and particle physics students in the same program facilitated cross-field intellectual exchange and the sharing of resources needed by both groups, while the participation of the Duke high energy physics group in the program gives it an international component.

Through introductory lectures and direct research involvement, the students gain experience and insights in the main stages of scientific research in nuclear and particle physics:

- The development of concepts to probe specific features of nuclear matter, particles and fields;
- The design, construction, testing, and installation of equipment and instrumentation;
- Data acquisition, analysis, and interpretation; and
- The dissemination of research results.

In addition to direct involvement in research projects, the REU program at Duke includes activities that are designed to broaden the students' physics foundation, enhance their research skills, and build confidence. These activities include: (1) regular meetings with the program coordinator, (2) research tutorials and special topic lectures, (3) a science writing tutorial, and (4) a required report and presentation by each student at the end of the program. The research reports written by the students form the main body of this document.

Personnel

2019 TUNL REU Participants

<i>Student</i>	<i>Home Institution</i>	<i>Faculty Advisor(s)</i>	<i>Class</i>
Emmanuel Aneke	Georgia Institute of Technology	Albert Young	Jr
Robert Bradford	Wake Forest University	Kent Leung	Jr
Sergi Castells	University of Illinois at Urbana-Champaign	Nicolo de Groot	Jr
Brittney Contreras	University of Tennessee - Knoxville	Amber Lauer	Jr
Emily Lynn	Taylor University	Ayana Arce, Katherine Pachal	Jr
Matthew McEaney	College of William & Mary	Anselm Vossen	Jr
Talisi Meyer	Simmons University	Calvin Howell, Collin Malone	Jr
Hannah Nelson	North Park University	Ashutosh Kotwal	Jr
Thomas Richards	University of Alabama	Kate Scholberg	Jr
Duncan Rocha	Harvey Mudd College	James Beacham	Jr
Emily Smith	Brigham Young University - Idaho	Robert Golub	Jr
Kaylisa Wolsey	Brigham Young University - Idaho	Sean Finch	Jr
Erem Ujah	North Carolina Central University	Diane Markoff	Fr

2019 TUNL REU Administration

Principal Investigator and Program Director:

Dr. Alexander Crowell

Co-Principal Investigator and CERN Experience Director:

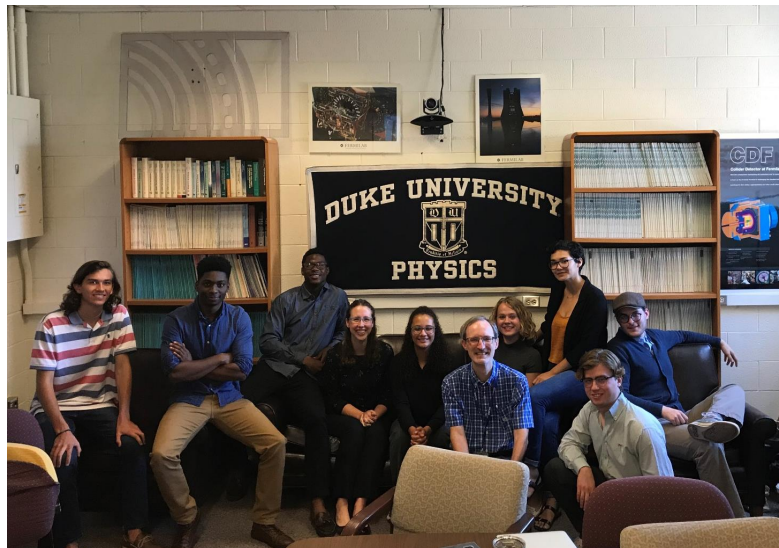
Professor Ayana Arce



PARTICIPANTS IN THE 2019 TUNL RESEARCH EXPERIENCES FOR UNDERGRADUATES (REU) PROGRAM. SHOWN IN THE PHOTOGRAPH FROM LEFT TO RIGHT ARE: (FRONT ROW) DUNCAN ROCHA (HARVEY MUDD COLLEGE), EMMANUEL ANEKE (GEORGIA TECH); (SECOND ROW) TALISI MEYER (SIMMONS UNIVERSITY), HANNAH NELSON (NORTH PARK UNIVERSITY), EMILY LYNN (TAYLOR UNIVERSITY), KAYLISA WOLSEY (BRIGHAM YOUNG UNIVERSITY - IDAHO); (THIRD ROW) EMILY SMITH (BRIGHAM YOUNG UNIVERSITY - IDAHO), HANK RICHARDS (UNIVERSITY OF ALABAMA), SERGI CASTELLS (UNIVERSITY OF ILLINOIS), BRITTNEY CONTRERAS (UNIVERSITY OF TENNESSEE); (TOP ROW): EREM UJAH (NORTH CAROLINA CENTRAL UNIVERSITY), MATTHEW MCENEANEY (WILLIAM AND MARY), ROBERT BRADFORD (WAKE FOREST UNIVERSITY).

Research Based at Duke

Chapter 1



1.1 Finding a Material with a Low Energy Threshold for Charged–Current Neutrino Interactions

T. RICHARDS, *University of Alabama, Tuscaloosa, AL*; KATE SCHOLBERG, *Duke University, Durham, NC*

We calculated the thresholds for charged–current electron neutrino and antineutrino interactions for most of the stable isotopes. Looking at the isotopes with the lowest thresholds, we found that ^{181}Ta and ^{160}Gd are reasonable candidates for low–threshold neutrino detectors, with thresholds at 0.188 MeV and 0.105 MeV respectively. These materials are both metals, have relatively high natural abundance, and are not frequently found in conjunction with radioactive substances, making them potentially viable for this task. Using the SNOwGLOBES software library, we computed estimated cross sections and event rates for supernova fluxes in these two materials.

Neutrinos are uncharged elementary particles, which interact only by the weak interaction under the Standard Model of particle physics. Therefore, neutrino interactions are rare and require sophisticated technology for detection. For this project, we were concerned with finding a suitable isotope for detecting charged–current (CC) neutrino interactions (see Fig. 1.1).

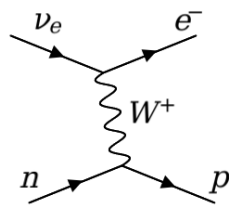


Figure 1.1: An electron neutrino charged–current interaction. An incoming neutrino (ν_e) interacts weakly with a neutron (n) via the passing of a virtual W^+ boson. The resultant particles are an electron (e^-) and a proton (p). Because the mediating boson, a W^+ in this case, is charged, the interaction is said to involve a “charged current.”

CC interactions manifest themselves in two modes: neutrino (Eqn. 1.1) and antineutrino (Eqn. 1.2).

$$\nu_e + (N, Z) \longrightarrow e^- + (N-1, Z+1) \quad (1.1)$$

$$\bar{\nu}_e + (N, Z) \longrightarrow e^+ + (N+1, Z-1) \quad (1.2)$$

There is a minimum energy an incoming neutrino must carry in order for a charged–current interaction to occur, given by:

$$E_{\text{thresh}} = \frac{M_f^2 + m_l^2 + 2M_f m_l - M_i^2}{2M_i}. \quad (1.3)$$

We used the National Nuclear Data Center’s “Nuclear Wallet Cards” database [Tul11] in conjunction with a Python interface for accessing the parameters [Hyk11]. Using our own Python script, we looped through most of the stable isotopes, grabbing the parameters necessary for calculating the reaction threshold using Eqn. 1.3 for neutrino and antineutrino modes separately. We then tabulated our results and sorted the isotopes by increasing threshold.

Looking at some of the lowest neutrino interaction energy threshold isotopes, we honed in on two that seemed like good candidates for neutrino detectors, ^{181}Ta and ^{160}Gd . We selected these isotopes for further study based on their practical properties; they are both metals, have reasonably high natural abundance, and are not usually found in conjunction with radioactive material.

Using the SNOwGLOBES library [Alb18], we estimated cross sections (see Fig. 1.2 and Fig. 1.3) and event rates (see Fig. 1.4 and Fig. 1.5) for neutrino interactions in these two materials.

The SNOwGLOBES software package relies on the GLOBES library, which is used for simulating long baseline neutrino oscillation experiments [Hub04]. SNOwGLOBES allows the user to configure simulation parameters, such as detector material and size,

for a particular experimental setup. There are a variety of scripts in the package for estimating interaction cross sections and event rates as functions of incoming neutrino energy. Because SNOwGLOBES is designed to make generalized calculations, its estimates could deviate significantly from actual values. In reality, cross sections are much more elaborate to calculate theoretically, but the utilities of SNOwGLOBES are sufficient for greenlighting the materials we studied.

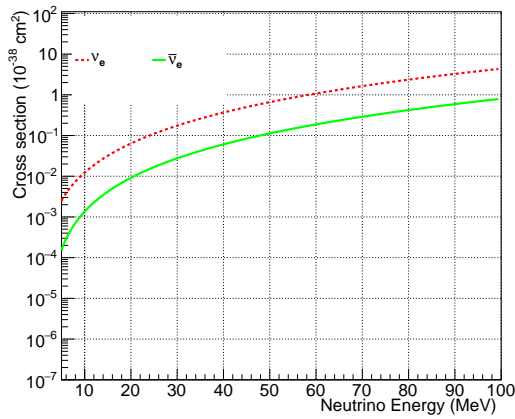


Figure 1.2: The estimated cross sections for ^{181}Ta for neutrino and antineutrino modes, calculated using SNOwGLOBES.

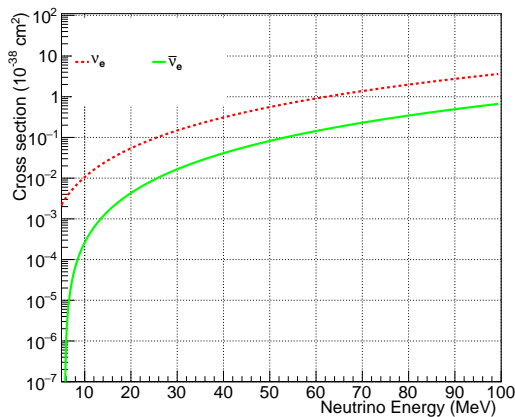


Figure 1.3: Similar to Fig. 1.2 but for ^{160}Gd .

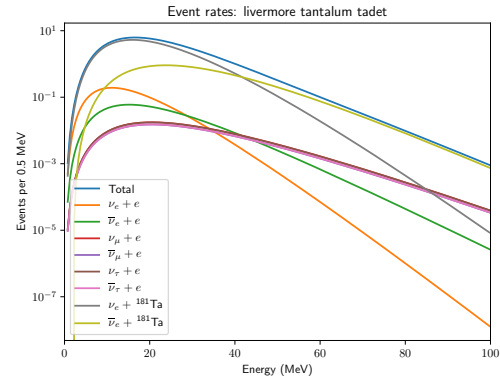


Figure 1.4: The estimated rates of various kinds of neutrino interactions. In this project, we are primarily concerned with the $\nu_e + ^{181}\text{Ta}$ curve, which is in gray.

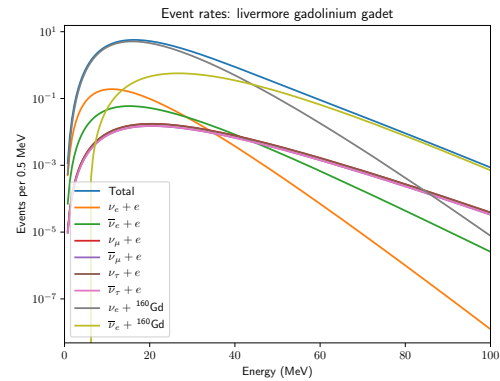


Figure 1.5: Similar to Fig. 1.4 but for ^{160}Gd

Now that we have some preliminary expectations for how these two materials behave, we want to look at neutrino interactions with simulated versions of these materials in detector configurations. We intend to use GEANT4 for these simulations. Our goal is to calculate how expensive a viable detector would be and determine whether it would be realistically feasible to build for an experiment.

[Alb18] J. Albert and A. Beck, 2018, <https://github.com/SNOwGLOBES/snowglobes>.

[Hub04] P. Huber, M. Lindner, and W. Winter, (2004), arXiv:hep-ph/0407333.

[Hyk11] J. M. Hykes, 2011, <https://github.com/jhykes/nuclide-data>.

[Tul11] J. K. Tuli, 2011, <https://www.nndc.bnl.gov/wallet/wccurrent.html>.

1.2 Sensitivity Study to Identify Important Nuclear Reactions in X-Ray Burst Nucleosynthesis

B. CONTRERAS, *University of Tennessee, Knoxville, TN*; AMBER LAUER, *TUNL*

When neutron stars in a low mass x-ray binary system collect matter from their H or He rich companion star, nuclear burning can occur on the high temperature and pressure surface. If a critical accretion rate is reached, it can cause the nuclear reactions to run away, resulting in an X-Ray Burst (XRB). By studying the sensitivity of XRB models to different nuclear reactions, we can help identify which are most important in the burst process. The stellar model used for this study was of an XRB in Modules for Experiments with Stellar Astrophysics (MESA) with a co-processed nuclear network. A single stellar model was rerun once for each nuclear reaction and its inverse in the network, varying its reaction rate by 100. The models with the greatest change indicate reactions that are key to XRB nucleosynthesis. Preliminary results identified 5 significant nuclear reactions. While the study is in its preliminary stage, it has proved capable of highlighting reactions that significantly affect XRB properties.

X-ray Bursts (XRBs) are some of the most energetic phenomena in the cosmos. When the H and He rich companion of a neutron star in a binary system for some reason expands beyond its Roche lobe (see Fig. 1.6), the H and He is fed into the neutron star, creating an accretion disk and ultimately accumulating on the surface. Due to the extreme temperature and pressure in the neutron star, H or He burning can occur. If a critical accretion rate is reached then it can result in runaway nucleosynthesis reactions, producing the XRBs that we wish to study. The nuclear burning is dominated by the (α, p) process during the early part of the burst, followed by the r-p process, which continues up the proton rich side of the chart of nuclides, up to around $A=100$, and then β -decays back to stability.

These bursts can give us many insights into the properties of the neutron star and how matter behaves at extremely high densities. Furthermore, conducting XRB sensitivity studies helps identify important nuclear reactions within these bursts, thus guiding experimental nuclear astrophysics. Such a study, in our case, consists of a computational stellar model of XRBs with coprocessed nuclear networks, meaning the nuclear network equations are coupled into each computational step. The model is run several thousand times, changing a reaction rate and its inverse by

a factor of 100 each time. Meaningful quantities are then derived from the model results and compared to the original (baseline) model.

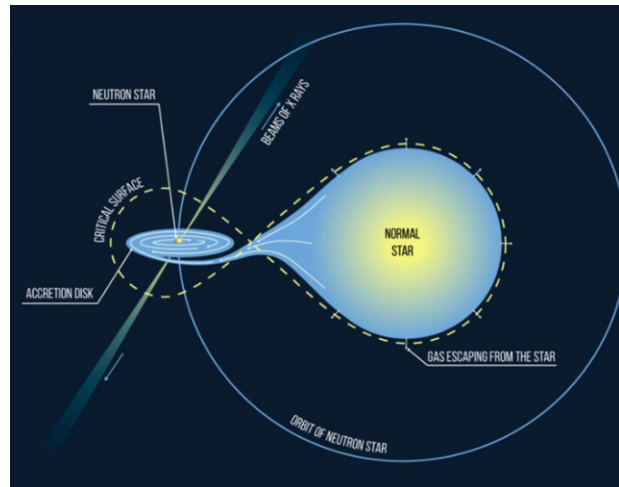


Figure 1.6: Visual of an accreting neutron star in an X-Ray Binary with a normal star whose Roche lobe is defined by yellow dashes [MIP16].

This project utilized two output data files from the models: the profile, a snapshot of the star at a

given time, and the history file, which provides information on the evolution of the star over time. The profile includes the mass fractions for 305 isotopes for each zone of the neutron star and the zone's mass (see Fig. 1.7). With this information a Python script was written to find the average mass fraction for each isotope, weighting by the zone's mass since contributions may vary. These averages were then compared with the corresponding isotopic mass fractions of the base model, ultimately producing a table of abundances for every reaction. The region of interest was zones in the photosphere since this is what can be compared to experimental data.



Figure 1.7: Concept visual of the composition of a 1D stellar model for a neutron star broken up into different zones.

We then expanded our script to analyze the history file, which contained luminosity and energy as a function of star age. With this information, we could plot luminosity vs. star age to produce XRB luminosity curves and find our burst frequency (see Fig. 1.8).

Since most of the models produced successive bursts, we also found an average burst for each model and from here, we intend to find integrated and maximum luminosity and energy, which can further provide us with our integrated burst luminosity variation, a metric defined to be:

$$M_{LC}^i = \int |\langle L_i(t) \rangle - \langle L_0(t) \rangle| dt \quad (1.4)$$

All of these quantities can then be compared to those of the baseline model, highlighting reactions with high variation and thus potential importance to XRB nucleosynthesis.

While the integrated values are still being calculated, and our change in the reaction rate by 100 is outside the scope of realistic uncertainties, the study was an initial iteration to illuminate reactions that may be crucial for XRB properties. Our preliminary results identify five nuclear reactions whose burst frequency changed significantly from the baseline (see Fig. 1.9). The high variations in burst frequency of

these reactions, in the extreme, shows the capability of our analytical methods in identifying the possible important nuclear reactions that we seek after.

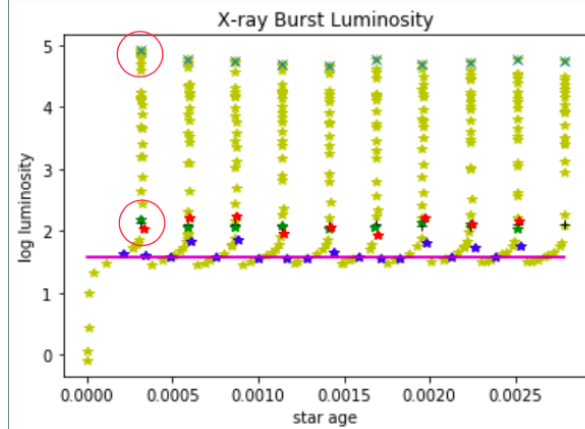


Figure 1.8: Single model luminosity curve (yellow *) with start (green *) and stop (red *) points of XRB activity. The curve includes peak location (cyan X), average baseline (magenta) and luminosity points closest to average baseline (blue *). Star age is given in years and luminosity is relative.

Reaction	Change in Burst Frequency (Δ BF)(s)
$^{94}\text{Ag}(n,\lambda)^{95}\text{Ag}$	61.28
$^{95}\text{Ag}(n,\lambda)^{96}\text{Ag}$	56.33
$^{96}\text{Ag}(n,\lambda)^{97}\text{Ag}$	50.16
$^{58}\text{Cu}(n,\lambda)^{59}\text{Cu}$	99.78
$^{61}\text{Cu}(n,\lambda)^{62}\text{Cu}$	53.67

Figure 1.9: Table of nuclear reactions with significant change in burst frequency from the baseline

After we complete our analysis of the integrated quantities for luminosity and energy, we hope to apply these same analytic methods to further runs with more refined reaction rate uncertainties. In doing so, we are improving upon similar studies that were done in the past when stellar modelling and nuclear network capabilities were less advanced [Cyb16].

[Cyb16] R. Cyburt *et al.*, *Astrophys.J.*, **55**, 830 (2016).

[MIP16] https://mipt.ru/english/news/x_ray_pulsars_fade_as_propeller_effect_sets_in, 2016.

1.3 Evaluating the Possibility of Reconstructing Polarized Λ^0 Hyperons in CLAS12 at Jefferson Lab

M. McENEANEY, *College of William & Mary, Williamsburg, VA*; A. VOSSEN, *Duke University, Durham, NC*

Λ^0 hyperons can be produced from hadronization of a struck quark in Semi-Inclusive Deep Inelastic Scattering (SIDIS). This process is of interest because the Λ^0 hyperon polarization may be inferred from its self-analyzing weak decay. Such probes allow one to extract information about the polarization of the constituent quarks within the proton and provide a test of fundamental aspects of Quantum Chromodynamics (QCD). In this study, we generated SIDIS events using a Lund Monte Carlo and simulated the response of the CLAS12 detector at Jefferson Lab's Continuous Electron Beam Accelerator Facility (CEBAF) using GEANT4 with different toroidal magnet field strengths and configurations (either inbending or outbending). We then processed events using the CLAS12 reconstruction framework to find the optimal configuration and maximize our reconstruction efficiency from the $\Lambda^0 \rightarrow \pi^- + p^+$ decay channel. For Λ^0 hyperons coming from a struck quark ($x_F > 0$), we obtained our best reconstruction efficiency in the low field outbending toroidal configuration.

Only about one third of the proton's spin may be explained from the spin of its constituent quarks, so it is a point of interest to be able to measure the transverse momentum of the quarks within the proton. One of the proposed methods to extract the necessary information from SIDIS processes is the use of a polarized probe such as the Λ^0 . The polarization of Λ^0 hyperons may be inferred from the distribution of the products of their self-analyzing weak decay (typically $\Lambda^0 \rightarrow p^+ + \pi^-$). Thus, Λ^0 hyperons could be very useful in studying polarization dependent effects of the strong force in hadron formation. For instance, being able to reconstruct the polarization of final-state hadrons would allow one to study spin-orbit correlations in fragmentation [Vos18]. Furthermore, measurement of the polarizing fragmentation function D_{1T}^\perp from polarized Λ^0 production would provide a test of the gauge structure of QCD since it is a naive time-reversal odd (T-odd) Transverse Momentum Dependent (TMD) probability distribution function [Boe18].

Jefferson Lab's accelerator delivers a polarized 11 GeV electron beam to the CEBAF Large Acceptance Spectrometer (CLAS12) in experimental Hall B where the beam encounters an unpolarized H_2 or D_2 target or a longitudinally polarized NH_3 or ND_3 target. Typical beam luminosity is $10^{35} \text{cm}^{-2} \text{s}^{-1}$. The CLAS12 apparatus is separated into a forward detector with polar angle coverage $5^\circ < \theta < 40^\circ$ and a

central detector with polar coverage $35^\circ < \theta < 125^\circ$. Both forward and central detectors have a azimuthal acceptance of about 360° [JLA08].

CLAS12 contains two superconducting magnets. In the central detector a superconducting solenoid with an average axial field strength of 5T is oriented along the beam line which provides momentum resolution and protects some of the detector equipment. In the forward detector is a superconducting toroidal magnet with its axis on the beam line and peak field strength of 3.6T which provides momentum resolution in the forward detector. The torus magnet may be run in either inbending or outbending configurations (negatively charged particles are either bent inward or outward). Both detectors have kinematic coverage $0.05 < x_{\text{Bjorken}} < 0.8$, $1.0 \text{ GeV}^2 < Q^2 < 10.5 \text{ GeV}^2$, and $W > 2.0 \text{ GeV}$ (to exclude elastic resonances) [JLA08].

For our study, we used a Lund Monte Carlo to generate 145,000 SIDIS events filtered for Λ^0 hyperons and 500,000 unfiltered events. We simulated the CLAS12 detector response with GEant4 Monte Carlo (GEMC 4.3.0) for four different toroidal configurations: inbending and outbending field at 75% and 100% field strength each to find the best configuration for maximizing the reconstruction efficiency from the $\Lambda^0 \rightarrow \pi^- + p^+$ decay channel. We then processed or "cooked" the output data with the CLAS12 reconstruction framework COATJAVA (5c.8.0 for filtered

events and 6b.3.0 for unfiltered).

To identify Λ^0 hyperons, we compared the tracks of all $\pi^- + p^+$ pairs in the reconstruction to known Λ^0 decay product tracks in the Monte Carlo truth for each combination of field strength and toroidal field configuration. We looked for reconstructed decay pair tracks either by requiring specific Lund PID numbers for the π^- and p^+ or by looking at π^- and all positively charged particles, both with and without requiring a kaon in the event. To qualify as a Λ^0 , decay pairs had polar and azimuthal angles within a 5° tolerance and momenta within a $0.1\text{GeV}/c$ tolerance of Monte Carlo truth tracks.

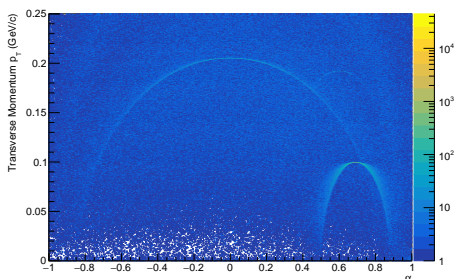


Figure 1.10: Armenteros-Podolanski Monte Carlo Background: The Λ^0 appears as the small ellipse at positive α since the p^+ is much heavier than the π^- . K_S^0 which decays to a symmetric π^-/π^+ pair appears as the larger ellipse centered over $\alpha = 0$.

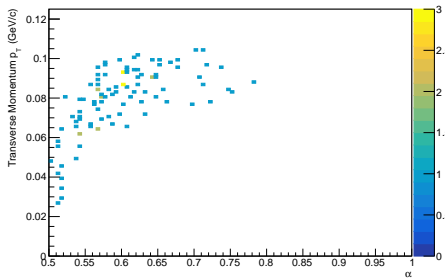


Figure 1.11: Armenteros-Podolanski Reconstruction: We see only the top left edge of the Λ^0 ellipse in the reconstruction.

By looking at the kinematic distributions of the decay products we determined optimal cuts to discriminate signal and background. The Monte Carlo background is shown in Fig. 1.10 along

with the Armenteros-Podolanski distribution for reconstructed Λ^0 hyperons in Fig. 1.11. We used Armenteros-Podolanski plots to restrict the transverse momentum p_T of the decay products relative to the Λ^0 between $0.025\text{ GeV}/c < p_T < 0.105\text{ GeV}/c$ and the longitudinal momentum asymmetry of the oppositely charged decay products $\alpha = \frac{p_i^+ - p_i^-}{p_i^+ + p_i^-}$ between $0.5 < \alpha < 0.8$. Furthermore, from the reconstructed energy and momenta of the two decay products, we computed invariant mass m and cut it to be within the window $1.108\text{ GeV}/c^2 < m < 1.122\text{ GeV}/c^2$ around the the Λ^0 mass which is sharply peaked around $1.1157\text{ GeV}/c^2$. Fig. 1.12 shows a plot of our reconstructed invariant mass signal and background. Finally, we required $x_{\text{Feynman}} > 0$ where $x_F = \frac{p_z}{p_{z_{max}}}$ is the ratio of the z-component of the produced hadron momentum to the maximum possible value of the z-component of the momentum based on the energy of the scattered lepton. This quantity is frame invariant and positive values indicate the hadron was produced in the current fragmentation region from the struck quark, whereas a negative value indicate the hadron comes from hadronization of recoil quarks.

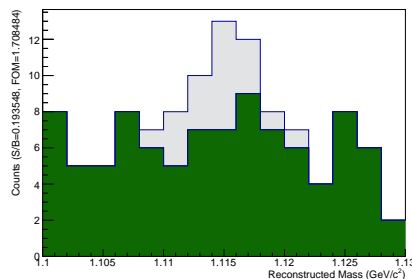


Figure 1.12: Reconstructed Mass ($x_{\text{Feynman}} > 0$): $S/B = 0.27$ and $FOM = 2.0$. The grey is the Λ^0 signal stacked on top of the green background from all p^+/π^- pairs in the reconstruction.

For Λ^0 hyperons from the current fragmentation region ($x_F > 0$) in both filtered and unfiltered events, we obtained the best reconstruction efficiencies without a kaon tag in outbending toroidal configurations. With the inbending configuration, we lost most π^- decay products in the reconstruction past the 5° acceptance of the forward detector, which was expected because the p^+ is much heavier than the π^- and the p^+ carries most of the Λ^0 momentum from the up and down quarks. Field strength had negligible effect

on our efficiency. Λ^0 reconstruction efficiencies for filtered and unfiltered events are presented in Tables 1.1 and 1.2 respectively. With 20% of approved CLAS12 run time and full beam luminosity at $10^{35}\text{cm}^{-2}\text{s}^{-1}$ we estimate we could see on the order of $10^5\Lambda^0$ hyperons in CLAS12.

In summary, we found that an outbending toroidal field configuration is optimal for maximizing Λ^0 reconstruction efficiency in CLAS12. We also found that field strength had negligible effect on this reconstruction efficiency. Further work would involve analyzing real data to see if Λ^0 polarization may be accurately reconstructed.

Table 1.1: Filtered Event Efficiencies, using PID ($x_F > 0$)

Torus Field	Λ^0	p^+	π^-
-1.00	0	0.016	0.00029
-0.75	0.000052	0.021	0.00038
0.75	0.0011	0.027	0.0083
1.00	0.0010	0.024	0.0061

Table 1.2: Unfiltered Event Efficiencies, using PID ($x_F > 0$)

Torus Field	K^+ tag	Λ^0	p^+	π^-
0.75	yes	0.000026	0.0064	0.0020
1.00	yes	0.000077	0.0055	0.0011
0.75	no	0.00050	0.063	0.021
1.00	no	0.00050	0.056	0.012

[Boe18] D. Boer *et al.*, (2018), <https://arxiv.org/pdf/1008.3543.pdf>.

[JLA08] *CLAS12 Technical Design Report, Version 5.1*, Technical report, Thomas Jefferson National Accelerator Facility, 2008, https://www.jlab.org/Hall-B/clas12/_tdr.pdf.

[Vos18] A. Vossen, (2018), <https://arxiv.org/pdf/1810.02435.pdf>.

1.4 Measurements of $^{124}\text{Sn}(\gamma, n)$ and $^{169}\text{Tm}(\gamma, n)$ Cross Sections at 13 MeV

K. WOLSEY, *Brigham Young University-Idaho, Rexburg, ID*; J.A. SILANO, A.P. TONCHEV, *Lawrence Livermore National Laboratory, Livermore, CA*; S. FINCH, W. TORNOW, I. TXORSE, *TUNL*

Nuclear data for photo-nuclear reactions is scarce. By using the activation technique, (γ, n) cross sections can be measured to a high precision. $^{169}\text{Tm}(n, 2n)$ is a common neutron monitor reaction, but there is no available data on its photo-nuclear counterpart, the $^{169}\text{Tm}(\gamma, n)$ reaction. Measurement of this reaction would allow use of thulium as a standard γ -ray monitor. Thulium, tin, and gold samples were irradiated by monoenergetic γ rays provided by the High Intensity γ -ray Source (HI γ S), located at Duke University. The resulting activity was quantified using γ -ray spectroscopy with high purity germanium (HPGe) detectors. The data confirmed the literature half-lives of ^{196}Au , ^{123m}Sn , and ^{168}Tm as 6.16 d, 40.1 m, and 93.1 d, respectively. Cross sections were extracted for the $^{124}\text{Sn}(\gamma, n)^{123m}\text{Sn}$ and $^{169}\text{Tm}(\gamma, n)^{168}\text{Tm}$ reactions, representing the first measurements of these reactions.

The cross section for any experiment in which a beam of particles is directed at a target is equal to the number of interactions or counts per unit time divided by the beam flux. However, variables such as self-absorption factor, half-life, γ -ray intensity, and other additional corrections must also be considered [Tor14]. The cross section for a reaction can be calculated with the following simplified equation:

$$\sigma \propto \frac{N_{\text{counts}}}{\Phi_{\text{beam}} N_o \epsilon t}. \quad (1.5)$$

In this experiment, the number of counts in a photo peak (N_{counts}), the number of target particles (N_o), beam flux (Φ), detector efficiency (ϵ), irradiation time (t), and other smaller corrections were measured. The motivation for this experiment was to determine the cross sections for the following reactions: $^{169}\text{Tm}(\gamma, n)^{168}\text{Tm}$ with a 93.1 day half-life and $^{124}\text{Sn}(\gamma, n)^{123m}\text{Sn}$ with a 40 minute half-life [Luo14]. Gold has been the standard reference cross section for γ -ray reactions but due to its high cost, there is a need for a cheaper, equally efficient standard reference. Thulium is a strong candidate as it has always been a standard reference for neutrons through the $^{169}\text{Tm}(n, 2n)^{168}\text{Tm}$ reaction, but never before has it been used as one for γ rays through the $^{169}\text{Tm}(\gamma, n)^{168}\text{Tm}$ reaction. Performing these measurements on thulium gives the data required to use it as a flux monitor for other γ -ray facilities.

Tin, on another hand, has the most stable iso-

topes of any element. Previous experiments have taken advantage of that property and measured reactions on tin by detecting outgoing neutrons, a technique not sensitive to the ground and isomeric states of ^{123}Sn and one that requires more complicated analysis procedures. Performing these measurements on tin give the first data of this reaction using the activation technique.

The setup of the experiment was simple, as shown in Figures 1.13 and 1.14. The target samples were counted before being irradiated, then irradiated by γ -rays provided by HI γ S, and finally the activity of the samples as they decayed was measured by HPGe detectors. The data recorded was analyzed using γ -ray spectroscopy.

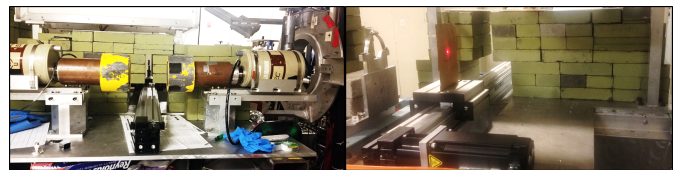


Figure 1.13: Photos of the irradiation setup at HIGS. The left panel shows the target in front of our HPGe detectors. The right panel shows the location of the γ -ray beam and the 1-m track used to move the target from irradiation to counting positions.



Figure 1.14: Photos of the setup in the low background counting facility in the basement of the Physics Building at Duke.

Another important part to the experiment was the development of the RApid Belt-driven Irradiated Target Transfer System (RABITTS), a motorized system to transfer targets from irradiation to counting positions. The system consists of a belt, pulley, and tensioning drive system that provides repeatability and a guidance system that provides accuracy of position and location for any attached target [Giv70]. Several control boxes were wired and built for this project, each consisting of a servomotor control module with a live feedback loop, a power shutoff switch/main power disconnect, a breaker, a 24 DC volt power supply, and 2A fuses. The RABITTS was set up in HI γ S and lead shielding was added where necessary to prevent radiation damage to the detectors. Gamma-ray induced reactions on ^{238}U , ^{235}U , and ^{124}Sn on the 1-m track at HI γ S were performed.

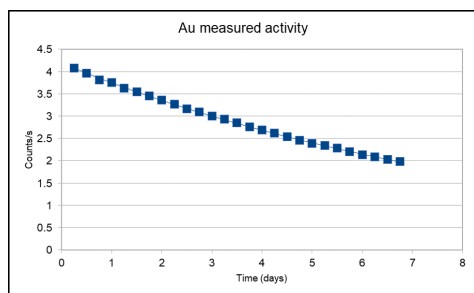


Figure 1.15: A plot of the observed activity for a gold target. We measured the half life to be 6.22 ± 0.06 d compared to the literature value of 6.1669 ± 0.0006 d.

Analysis of the data used γ -ray spectroscopy. Gamma rays interact with the crystal in our detector

to produce peaks corresponding to the γ -ray energy. HPGe detectors were used because they have superior energy resolution, allowing the peaks in the spectrum to be distinguishable. The horizontal position of the peak is determined by the γ -ray's energy while the area of the peak is determined by the intensity of the γ ray and the efficiency of the detector. Using γ -ray spectroscopy we determined the half life of our gold standard foil as shown in Fig. 1.15. We also determined our detector efficiency using a mixed source as shown in Fig. 1.16.

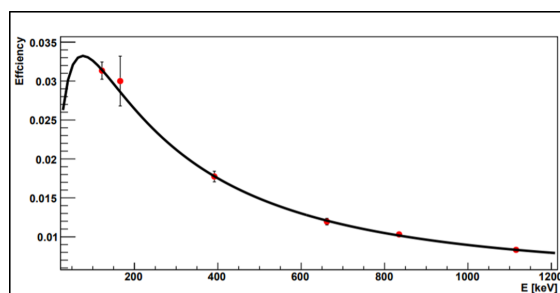


Figure 1.16: For detector efficiency determination, radioactive sources of known activity (^{241}Am , ^{109}Cd , ^{57}Co , ^{139}Ce , ^{113}Sn , ^{137}Cs , ^{54}Mn , ^{65}Zn) were used. They are plotted here and fit with a curved power law function [Gil08].

In conclusion, the data confirmed the literature half-lives of ^{196}Au , ^{123m}Sn , and ^{168}Tm as 6.16 d, 40.1 m, and 93.1 d, respectively. Cross sections were extracted for the $^{124}\text{Sn}(\gamma, n)^{123m}\text{Sn}$ and $^{169}\text{Tm}(\gamma, n)^{168}\text{Tm}$ reactions, representing the first measurements of these reactions.

Other experiments measured (γ, n) for both the ground and isomeric state of ^{123}Sn . As shown in Figure 1.17, the resulting cross section value for ^{123}Sn in this experiment is lower than previous experiments, indicating there is likely a small (γ, n) transition to the ground state. Our results are most likely due to some transition strength to the ground state, which wasn't expected because of the large spin difference. Since the experiment was not optimized to measure the ground state transition, further work plans to build on this experiment, redoing the experiment and quantifying the (γ, n) branching ratio to the ground and isomeric states.

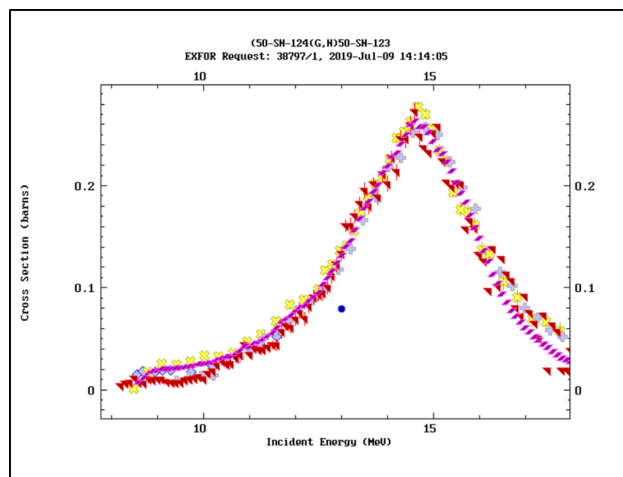


Figure 1.17: Previous cross section data for the $^{124}\text{Sn}(\gamma,n)^{123}\text{Sn}$ reaction [Uts11, Ful69, Dan14]. Our measurement is shown as the blue data point at 13 MeV.

[Dan14] A. Danagulyan *et al.*, *Yadernaya Fizika*, **77**, 1378 (2014).

[Ful69] S. C. Fultz *et al.*, *Phys. Rev.*, **186**, 1255 (1969).

[Gil08] G. Gilmore, *Practical Gamma-Ray Spectrometry*, Wiley, 2008.

[Giv70] W. Givens, W. Mills, and R. Caldwell, *Nucl. Instrum. Methods*, **80**, 95103 (1970).

[Luo14] J. Luo, L. An, and L. Jiang, *Nucl. Sci. Eng.*, **178**, 261267 (2014).

[Tor14] W. Tornow *et al.*, *Energy Dependence of Fission Product Yields for ^{239}Pu , ^{235}U , and ^{238}U* , Technical report, LANL, 2014.

[Uts11] H. Utsunomiya *et al.*, *Phys. Rev. C*, **84**, 055805 (2011).

1.5 Scrubbing System Supporting Tritium Gas Target for Research at HI γ S

T. MEYER, *Simmons University, Boston, MA*; C.R. HOWELL, C. MALONE, *TUNL*

Tritium, a radioactive isotope of hydrogen, will be the basis of experiment P-02-13 at HI γ S. This study will utilize a tritium gas target to obtain cross-section measurements of two- and three-body photodisintegration of the triton in order to further understand nuclear structure and reactions, specifically three-nucleon interactions. In order to reduce loss of the radioactive gas, safety systems will be implemented including a tritium scrubber system. This system will work in conjunction with a copper-zinc catalyst in order to utilize the reduction of copper to continuously transform elemental tritium into T₂O or HTO, allowing the tritiated water to be collected within a molecular sieve and safely disposed of. Reactions catalyzed by the CuZn bed were examined using a Residual Gas Analyzer at temperatures of 23°C to 200°C to measure isotope concentrations and compositions of the various gas streams that will flow through the scrubbing system during normal operation.

A 1.3 kCi tritium gas target will be the basis of experiment P-02-03 at the High Intensity Gamma-Ray Source (HI γ S) facility. This experiment will measure two emitted neutrons, i.e. the measurement of the ${}^3\text{H}(\gamma, nn)p$ reaction and obtain a kinematically complete measurement of the three-body photodisintegration of the triton to further understand three-nucleon interactions [How19]. Utilizing tritium allows the strong nuclear force to be studied unambiguously without the complications from the Coulomb interaction. Ultimately, the precision goal of this experiment is to measure neutron-neutron and neutron-proton final-state interactions within the nucleus to compare with previously calculated data of that outside the nucleus. With this target design, the protons cannot be detected at 20 MeV. Therefore, neutron-proton interactions will be measured by detection of the neutrons emitted to opposite sides of the beam axis. Fourteen detectors in total will be positioned with seven on either side of the beam axis to allow for this neutron detection. The original experimental set up can be seen in Fig. 1.18.

In order for this experiment to run continuously without risk of tritium release within the building, a redundant scrubbing system is necessary. This system will be modeled from that at the Laboratory for Laser Energetics at the University of Rochester [Shm13]. However, the system at HI γ S will utilize a copper zinc bed as the primary catalyst to account for oxygen within the air streams. The copper zinc bed will consist of a stainless-steel cylinder filled with copper pellets approximately 3 mm in diameter to

catalyze the oxidation of hydrogen and its isotopes to form tritiated water. This reaction will regenerate the copper bed and allow the process to continue.

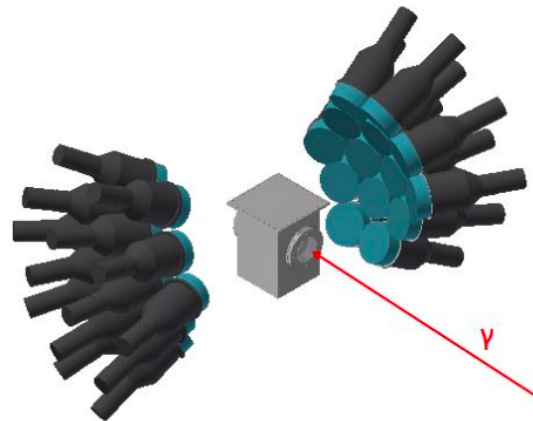
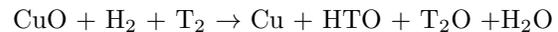


Figure 1.18: Three-dimensional rendering of the original target system setup. Although this rendering shows 14 detectors on either side of the beam line, only 14 detectors will be used in total with 7 detectors on each side. The target cell is located within the secondary containment chamber and is 5 cm long and pressurized with 12 atm of tritium gas.

Other components of the scrubbing system include: two molecular sieve beds to absorb tritiated water and protect downstream beds, a nickel bed to

crack organic components, and a zirconium iron bed to scrub elemental tritium in the event of a large leak. The scrubbing system will connect to an airtight glovebox in which the tritium target will be held in a secondary containment chamber. During normal operation, air will be allowed to pass through the copper zinc bed and first molecular sieve before returning to the glovebox. However, in the event of a large leak of the target, the second molecular sieve, nickel bed, and zirconium iron bed will act as additional safety measures. This modeled system can be seen in Fig. 1.19 and the pathways of airflow can be seen in Fig. 1.20.

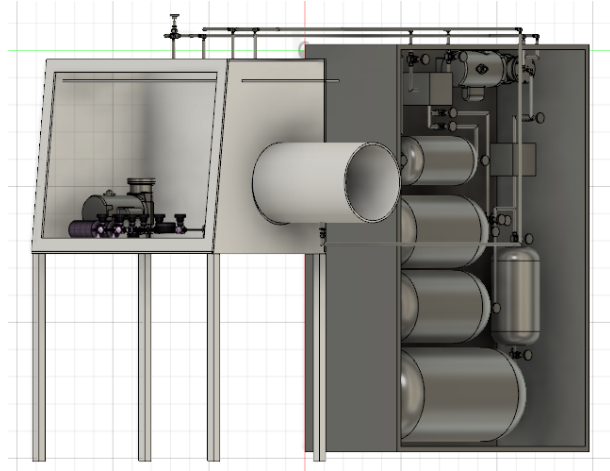


Figure 1.19: Glovebox containing secondary containment chamber (left) and scrubbing system (right).

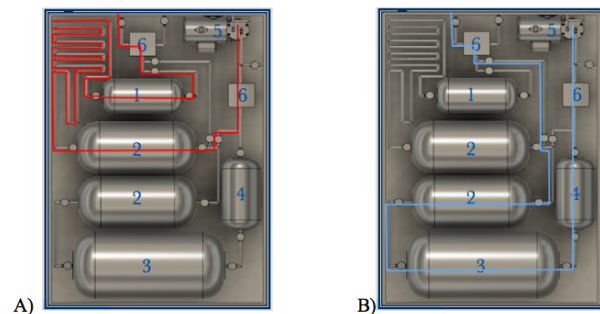


Figure 1.20: Components: 1. Copper Zinc Bed, 2. Molecular Sieve Beds, 3. Nickel Bed 4. Zirconium Iron Bed, 5. OTS Pump MB158, 6. Tritium Monitors A) Gas flow during normal operation B) Gas flow in the event of a large leak

Analysis of isotope concentrations and compositions was completed to further characterize the re-

actions catalyzed by the copper zinc bed as well as to find an optimal temperature for operation. This was done using a Residual Gas Analyzer SRS 100 at temperatures of 23°C, 80°C and 130°C. During this analysis, various gases were flowed through to model how they would be while the scrubbing system was in operation. Gas streams analyzed included hydrogen flowed in an air stream of helium or 1% oxygen in helium as well as 1% oxygen in helium alone which will be referred to as an oxygen load. Hydrogen was used in place of tritium as the two behave chemically the same despite being isotopically different. The various gas loads were first flowed through a bypass to be able to compare each scan to a background spectrum. Each test began and was followed with a hydrogen-helium purge to clean the system and remove residual gases. During all runs, hydrogen had a flow rate of 50 or 100 sccm while the helium and oxygen in helium possessed a flow rate of approximately 5 LPM.

Analysis of the oxygen loads at each temperature showed that complete saturation of the copper zinc bed took longer to reach at higher temperatures. This can be seen in Fig. 1.21 as the percentage of oxygen in the outlet stream is plotted over time. Higher temperatures also resulted in a lower percentage of hydrogen within the outlet stream of the system which would correspond to the levels of tritium passing through the system during operation. While 100% of the hydrogen was able to flow through at 23C, at 130C approximately 20% was seen.

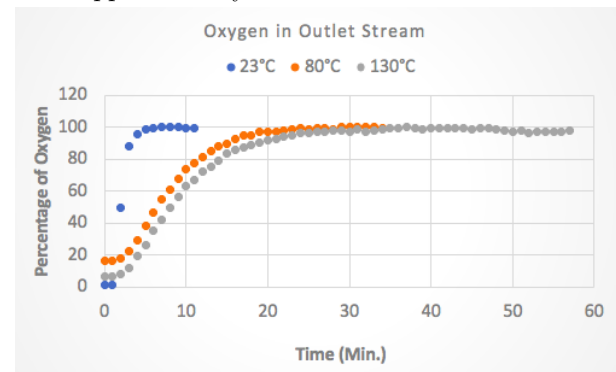


Figure 1.21: Percentage of oxygen in outlet stream over time based on Residual Gas Analysis.

Throughout this program, the design, construction and development of the tritium scrubbing system, specifically the copper zinc bed, were expanded. Residual gas analysis of the copper zinc bed verified its catalytic capability. This analysis also showed

the optimization of the oxidation of hydrogen and increased oxygen capacity at higher temperatures. Future work will continue to develop the tritium scrubbing system utilizing the copper zinc bed as the main catalyst.

[How19] C. Howell *et al.*, *Differential Cross-section*

Measurements of Two- and Three-body Photodisintegration of the Triton at 20 MeV, Technical report, Duke University, 2019.

[Shm13] W. Shmayda and S. Gnolek, *Catalytic Oxidation of Hydrogen in Air Streams*, Technical report, University of Rochester, 2013.

1.6 Preparations for Compton Scattering from Cryogenic Liquid ^3He at HI γ S

R.W. BRADFORD III, *Wake Forest University, Winston-Salem, NC*; K. LEUNG, *TUNL*

Low-mass nuclear Compton scattering projects at HI γ S are focused on determining experimentally the static electric (α_E) and magnetic (β_M) dipole polarizabilities of neutrons. Building on past experiments, the next iteration will use a liquid ^3He target volume to offer a new nuclear structure for analysis. This project is centered around preparing for the upcoming experiments. A new epoxy-lined gas storage tank was commissioned and sealed for the ^3He gas containment system. Leakage rates were measured, and a residual gas analysis was performed. The sealed tank was shown to have a leak rate of $< 2.0 \times 10^7$ mbar*L/sec and main contamination from water, nitrogen, and oxygen at levels that can be removed by internal systems. A computational model was constructed based on particle beam flux attenuation in scattering processes. Values of the contaminate ^4He level C_4 (along with the percentage uncertainty in this value $p(C_4)$), the percentage uncertainty in the cross section of the experimental scattering with ^4He $p(\sigma_4)$, and the experimental runtime T were varied to determine impact on the percentage uncertainty in the scattering cross section with ^3He . Optimal values (against cost) of T and $p(\sigma_4)$ were found to be 200h and 10% respectively for C_4 less than 10% and $p(C_4)$ less than 25%.

The static electric (α_E) and magnetic (β_M) dipole polarizabilities of neutrons, based on the response of internal charge distribution and spin alignments to applied electromagnetic fields, encapsulate information about the internal structure of nucleons. Since free-neutron decay prevents their measurement with the application of a static field, Compton scattering off low-mass nuclei allows for the measurement of these polarizabilities through the application of a dynamic electromagnetic field in the form of a monochromatic γ -photon beam. Past experiments with scattering from deuterons (^2H) [Mye14] have yielded values for α_E and β_M of neutrons (using established values for protons) that the current ^3He project hopes to improve upon. Additionally, a more recent ^4He scattering measurement at HI γ S [Sik17] provides a successful proof of concept using the facility and experimental apparatus. Measurement of scattering cross sections from differing nuclear structures and beam energies provides a varied data set from which to determine values.

The planned ^3He experiments will be based on the previously used ^4He cryogenic target system but will build on it in several ways. Bearing in mind the substantially rising cost of ^3He over the past decade, a robust gas handling and recovery system is being designed. A 120 gallon epoxy-lined tank was purchased for use as a ^3He storage vessel in the system. It was sealed at all ports with vacuum putty and leak

tested to a rate below $< 2.0 \times 10^7$ mbar*L/sec. Additionally, residual gas analysis was performed using an RGA SRS 100 system. Figure 1.22 shows results from this analysis. Main contaminant gases in the system are nitrogen, water, and oxygen at levels that internal traps and filters in the cryotarget can remove efficiently.

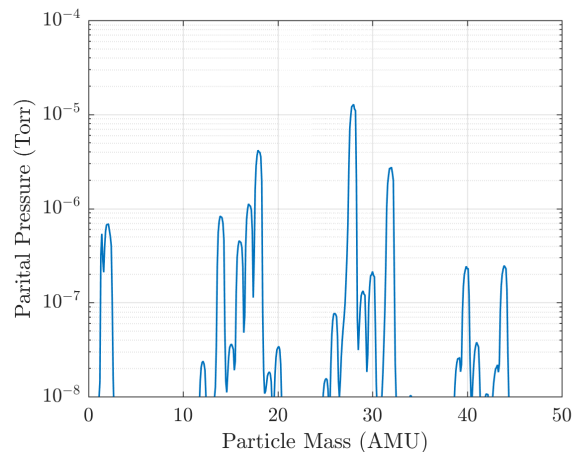


Figure 1.22: Plot of partial pressures in storage tank from residual gas analysis. Main peaks occur at and around 28 AMU (N_2), 18 AMU (H_2O), and 32 AMU (O_2). Scan was performed up to system limit at 100 AMU. Masses not shown had pressures below 10^{-8} Torr.

The experimental volume of ^3He will have a statistically relevant level of ^4He contamination. Perfect knowledge of this level and the differential Compton scattering cross section of ^4He at the experimental beam energy would allow for the prediction of scattering events from these nuclei in the target volume and therefore exact compensation in data analysis. However, as these values are not (and cannot be) known with perfect precision, they introduce a greater level of systematic uncertainty.

If a beam of particles enters a thin layer of material with thickness dz , the flux Φ (particles per area per time) of the beam will decrease by $d\Phi$ according to

$$\frac{d\Phi}{dz} = -n\sigma\Phi \quad (1.6)$$

where n is the number density of scattering centers in the target material and σ is the cross section of beam attenuating events. The value

$$P = -\frac{d\Phi}{\Phi} = n\sigma z \quad (1.7)$$

is therefore the probability that an incoming particle will scatter from the target material in z (assuming weak attenuation). Given a scattering target that is a mixture of ^3He and ^4He atoms,

$$\sigma_3 = \frac{N_{sc}}{n_3ITz} - \frac{n_4}{n_3}\sigma_4 \quad (1.8)$$

where N_{sc} is the total number of scattered particles in a time T , I is the intensity (particles per time) of the particle beam, σ_3 and σ_4 are the cross sections of scattering from ^3He and ^4He atoms respectively, and n_3 and n_4 are the number densities of ^3He and ^4He scattering centers in a target volume respectively. Since the number density of a component in a target volume can be related to its molar mass M , fractional number concentration C , and the target mass density ρ by

$$n = \frac{\rho C N_A}{M} \quad (1.9)$$

where N_A is Avogadro's number, Eqn. 1.8 can be rewritten

$$\sigma_3 = \frac{N_{sc}M_3}{\rho_3 C_3 N_A I T z} - \frac{M_3}{M_4 C_3} \sigma_4 + \frac{M_3}{M_4} \sigma_4 \quad (1.10)$$

where C_3 is the fractional concentration of ^3He , and M_3 and M_4 are the molar masses ^3He and ^4He atoms, respectively.

Using this definition, a standard simplification for propagation of uncertainty for nonlinear combinations was used to model error in the ^3He cross section and optimize with regard to experimental runtime and uncertainty in the ^4He cross section, as

these values remain controllable. The model took C_4 in the range 0-10 % and the percentage uncertainty in C_4 in the range 0-25%. Other values and their uncertainties were taken from descriptive literature of the experimental setup [Sik17, Ken16, Leu19]. Analysis showed significant change beginning where T was below 200 hours and percentage uncertainty in σ_4 was above 10%. This implies that these values represent the lowest precision such that main contributions to uncertainty were from other variables. Figure 1.23 shows the contour plot of the optimized case. These values in the plausible ranges of C_4 and $p(C_4)$ give a minimum uncertainty in σ_3 of about 2.4% and a maximum of about 2.8%.

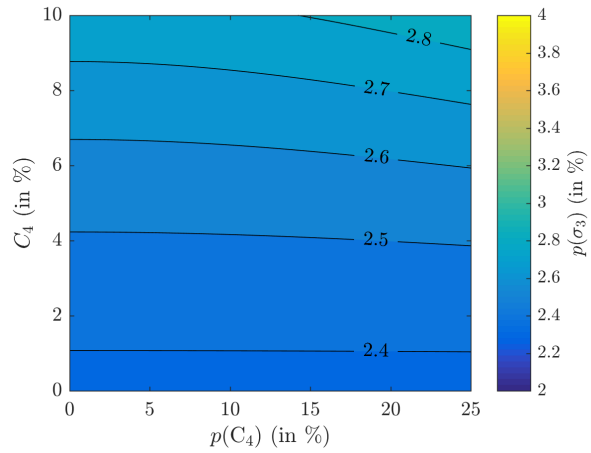


Figure 1.23: Contour plot of uncertainty in σ_3 for $p(\sigma_4) = 10\%$ and $T = 200\text{h}$. The shorthand $p(x)$ is used to represent the percentage uncertainty in the value x . This case shows the estimated uncertainty in the Compton scattering from ^3He with controllable variables optimized. These values in the plausible ranges of C_4 and $p(C_4)$ give a minimum uncertainty in σ_3 of about 2.4% and a maximum of about 2.8%

[Ken16] D. Kendellen *et al.*, Nucl. Instrum. Methods, **A840**, 174 (2016).

[Leu19] K. Leung, D. Haase, and D. Markoff, *^3He Cryotarget Gas Handling Systems*, 2019, Internal Document.

[Mye14] L. S. Myers *et al.*, Phys. Rev. Lett., **113**, 262506 (2014).

[Sik17] M. H. Sikora *et al.*, Phys. Rev. C, **96**, 055209 (2017).

1.7 Earth's Field Nuclear Magnetic Resonance

E. SMITH, *Brigham Young University - Idaho, Rexburg, ID*; R. GOLUB, *TUNL*

When a proton is placed into an external magnetic field, it will attempt to align its magnetic moment to that field. Then if that external magnetic field is suddenly turned off, the proton will start to precess around the only other magnetic field available, the Earth's. The goal of this project was to get an instrument operational that would take advantage of this concept. It would be used to find the spin relaxation time (T_2), a measure of the magnetic field gradients, of the sample. This would then be used to test the magnetization of other materials for a larger project. An Earth's field nuclear magnetic resonance control box and sample coil were used along with a sample of water (our proton source) to produce a waveform from the precession of the water molecules. From that waveform we were able to calculate our T_2 value. After many setbacks and multiple trials, we were successful in operating the instrument to produce waveforms in the correct shape and scale, thus getting a T_2 value that was close to the established value. While more testing and calibration is still needed, the instrument is now working and can be used in future testing of the magnetization of materials.

When placed into a magnetic field, a proton's magnetic moment will attempt to align itself with that field. However, the spin angular momentum causes the magnetic moment to precess around the magnetic field instead of aligning with it. If that magnetic field is suddenly turned off, the magnetic moment of the proton is left to precess around the Earth's magnetic field instead.

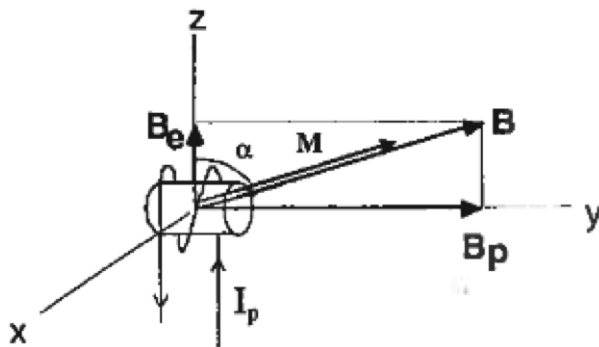


Figure 1.24: Representation of the Earth's Field technique [Inc13].

This concept can be extended to water molecules (an easily accessible source of single protons thanks to their hydrogen atoms). As shown in Fig. 1.24, when the magnetic field is turned on, the magnetization of the water sample aligns itself with the resultant B field. With B_p being so much larger (several hundred times) than the B_e , the resultant B field is almost per-

fectly aligned with the B_p field. When you turn off the B_p field quickly enough, the magnetization starts to precess around B_e . For this experiment, the B_p field will be produced by running current through the sample coil and that same coil will detect the precession of the atoms which will be visible on an attached oscilloscope.

Once the precession signal is visible, we can analyze the waveform for the spin relaxation time (T_2). This is a gradient of the field and has a well-established value of 2.5 s [Inc13] for water and thus is a good benchmark to check if the instrument is working. Once it is established the instrument is working, it can be used to find characteristics of the magnetization of other objects by placing them near the water sample which changes the T_2 gradient of the water. This technique could be used to determine the magnetization of materials used in the apparatus being constructed to look for the Neutron Electric Dipole Moment, which is very sensitive to gradients.

When the instrument was set up, it started producing waveforms as seen in the upper image of Fig. 1.25 when it should have been the shape of the lower image of Fig. 1.25. Analyzing the waveform in Excel, the slope of the peaks is given in an exponential equation in the form of Ae^{bx} . If this is taken and used with the basic T_2 equation $e^{-\tau/T_2}$, the equation for T_2 becomes $T_2 = \tau/b$. When this equation was applied to the generated waveform, the T_2 value was 10.97 ± 0.63 ms. As mentioned above, the value of

T_2 for water should be 2.5 s. In attempts to correct this, one of following variables was changed for each test: compass direction, shielding, position in the lab, sample of water, and location (inside vs. outside). Despite the assurance of the instruction manual that each of these variables should have had a measurable effect on the waveform and the T_2 value, none of them did.

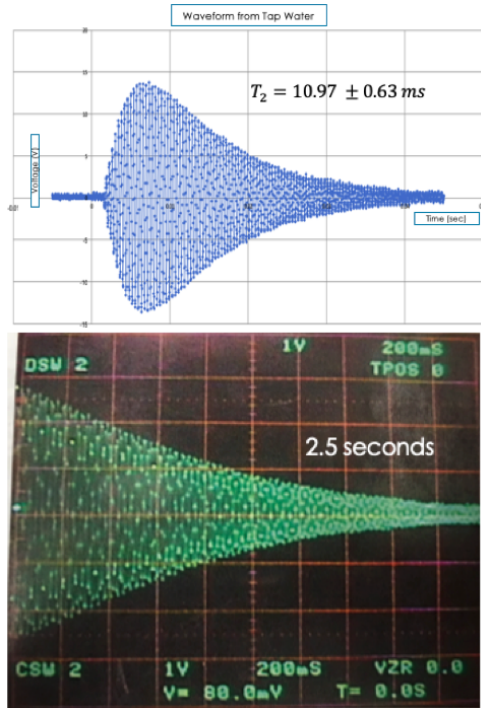


Figure 1.25: Upper: The generated waveform. Lower: The expected waveform.

As testing continued, the instrument was run with no sample present to establish if there was background noise influencing the shape of the waveform. That test produced an identical waveform to what had been assumed to be the signal from the water sample as shown in Fig. 1.26. Each waveform that was thought to have been being produced from an interaction with the sample of water throughout the entire experiment was some kind of background noise.

After troubleshooting each part of the instrument and coming up with no explanation as to why this was happening, we contacted the company who made the instrument. They answered saying this was the "Coil Transient" [Mel] and was a normal part of the instrument, it simply meant it wasn't tuned properly, and sent a new instruction manual.

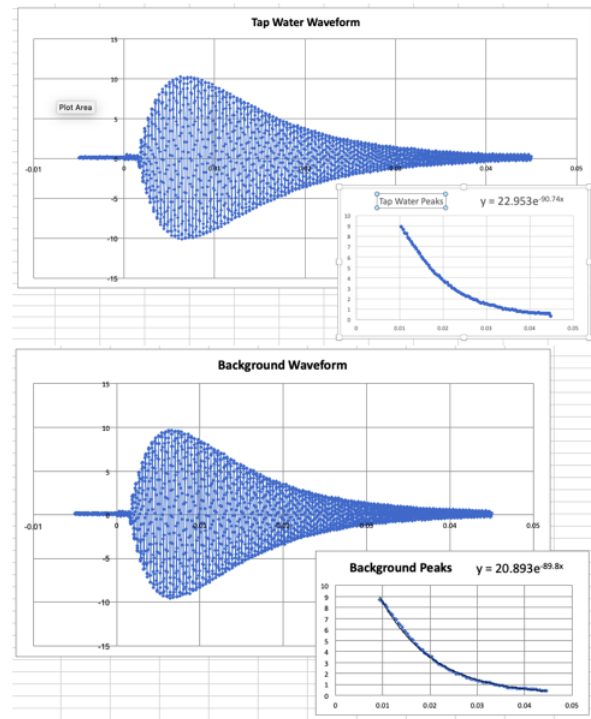


Figure 1.26: Upper: Waveform with a sample of tap water in the coil. Lower: Waveform with no sample in the coil.

Following the new instructions, the instrument was taken outside where the Earth's magnetic field is more homogeneous for the tuning process and data collection. The tuning process included obtaining an exact measurement of the Earth's magnetic field in the work area, taking a wave generator and an extra coil to tune the sample coil to the Earth's magnetic field, and then removing the extra coil and fine tuning the tuning of the sample coil by hand [Mel]. When this process was completed, we were able to record the waveform produced by the precession of the water molecules as seen in Figure 1.27. Calculating T_2 from these waveforms gives values of 0.25 – 0.50 s. While this still falls short of the established value of 2.5 s, it is much closer than the 10 ms we were calculating before from the background noise.

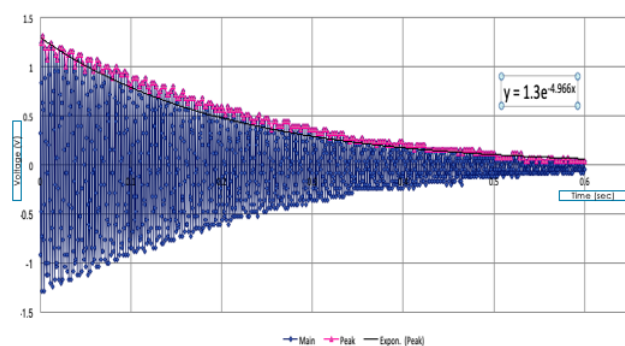


Figure 1.27: Waveform produced by a correctly functioning instrument.

In conclusion, despite multiple setbacks the

Earth's field nuclear magnetic resonance instrument is now functioning and has a set of instructions that allows for reproducible data. Further work on this project will include refining experimental techniques to improve the T_2 value and obtaining shielding that will allow the instrument to function within the lab so that it can be used to find the magnetization of other materials.

[Inc13] T. Inc., 2013, Earth's Field NMR Instructor's Manual.

[Mel] B. Melton, *Earth's-Field Nuclear Magnetic Resonance "A Conceptual Introduction to NMR"*, TeachSpin, EFNMR1-B Operating Manual.

1.8 Development of Pelletron Accelerator for High Precision Calibration of Silicon Detectors

E. ANEKE, *Georgia Institute of Technology, Atlanta, GA*; A.R. YOUNG, *TUNL*

We are developing a pulsed and tunable Pelletron accelerator to provide measurements of bremsstrahlung energy loss for next generation neutron beta decay experiments. The development of our Pelletron system is the first step before any measurements are made. The goals of our project are to improve the performance of an N_2 purge and implement a suppressor electrode to reduce arcing, understand possible sources of coronal discharge loss, make a first detection of the electron beam, and develop a test beam line. These first steps were successful, greatly reducing charge loss and arcing, and confirming the production of over 250 keV electron beams.

Neutron beta decay (NBD) is the decay of a neutron into a proton by the emission of an electron and electron anti-neutrino. The emitted electron can have any energy from 0 keV to 783 keV. The emitted electron energies are difficult to precisely measure because of bremsstrahlung, the emission of electromagnetic radiation produced by the deceleration of an electron hitting an atomic nucleus. For the next generation of beta decay measurements, the precision of current bremsstrahlung simulations is not sufficiently precise, motivating direct measurement of the bremsstrahlung loss to calibrate NBD electron energy measurements. We plan on using a Pelletron accelerator to make these direct measurements.

A Pelletron is a type of electrostatic accelerator that takes charge received from a moving chain of short conductive tubes (pellets) connected by nylon links. It is composed of two wheels, one wheel at high voltage and one down the column held at ground. A motor is connected to the wheels driving them to a speed of about 60 mph. Along the wheels are the aforementioned pellets, hence the name Pelletron. Along with the wheels and chain, there are two inductors, two suppressors, two pick-off wheels and a resistor chain (see Fig. 1.28).

To understand how the Pelletron works, consider the lifespan of a single pellet. First, above the grounded wheel, the first inductor induces a negative charge on the pellet. Then, as the pellet travels up the column, some of its negative charge is picked off and sent to a later location. The pellet continues to

travel with some of its charge and it reaches the first suppressor. The suppressor is a saddle shaped electrode that works to prevent the charge in the moving pellet from arcing to neighboring electronics or prematurely to the high voltage terminal wheel. Finally, the charge from the pellet is taken to the high voltage wheel.

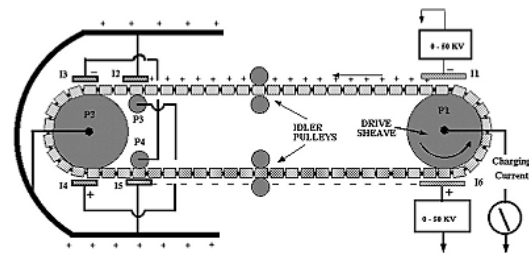


Figure 1.28: Schematic of the Pelletron Charging System.

Now, the whole process repeats but with different signed charges. The first pick-off node took some of the induced negative charge and it is used to supply negative charge to the second inductor. This inductor induces a positive charge on the pellets for the returning sequence. Then the second pick-off node pulls some of the positive charge from the pellets and uses it to supply charge to the first suppressor. Then lastly, the pellets are brought to the ground wheel after going through a negatively charged suppressor.

One way to understand the purpose of the Pel-

letron to think of it as essentially a current source. The pellets carry a charge that changes over time which is current by definition. The current flows through the resistor chain to the ground end making a voltage divider network that establishes the voltage drop down the accelerator column between the high voltage terminal and the grounded wheel.

The entire Pelletron system was immersed in a tent filled with N_2 gas (see Fig. 1.29). The N_2 gas was meant to be used as a dielectric gas to insulate all the high voltage in the system. We were also constantly purging the tent in attempts to lower the water vapor levels in the system, as this would contribute to the arcing. Because of the size of the tent (approximately $1.6m^3$), we would exhaust an entire standard gas tank in a 24 hour span and in turn, our levels of N_2 weren't optimal.



Figure 1.29: Pelletron System inside of tent.

Another issue was the loss of charge down the column. Between the two ends of the Pelletron, the grounded end and the high voltage terminal, lies the voltage divider network. Because the network of 28 resistors is biased, both ends should produce matching currents. However, ammeters on either ends of the resistor chain (one placed at the first resistor and another at the 28th resistor) would yield different currents. The terminal end current would always linearly increase with the inductor voltage, but the ground end current would plateau at around $2.5\mu A$. A stagnancy in the ground current would mean a stagnancy in the energy output of the beam. This was speculated to be another product of poor N_2 flow. It was also possible that there was an issue within the hardware of the resistor chain.

Lastly, there was no electron beam to be found. Previously, a silicon detector was mounted on the end

of the beam line but the detector did a poor job perceiving the beam. The silicon detector was mounted on insulators and in turn would build up charge. The electrons from the beam would steer away due to the Coulomb force and then we would see no beam in the detector.

In attempts to reduce the arcing, we needed a better system for a more consistent flow of dry N_2 into the tent. Our goal was to reduce the amount of water vapor in the system so the integrity of the environment was very important. Checking the tent for holes and potential openings was essential. Ultimately, we decided to switch from using standard gas tanks to using the evaporated nitrogen gas from a liquid nitrogen Dewar. This meant that we could purge for much longer periods of time at a higher flow rate and the concentration of H_2O tremendously decreased. We could now reach higher inductor voltages without arcing prematurely.

Next was the investigation of the inconsistent ground and terminal currents. Ultimately, the liquid nitrogen Dewar switch ended up fixing most of the charge loss but looking into the resistor chain was still necessary. In the resistor chain, there are 28 $1M\Omega$ resistors. While the accelerator was running, we would place a third ammeter at some resistor n , where $1 > n < 28$, to pinpoint the location of charge loss along the column.

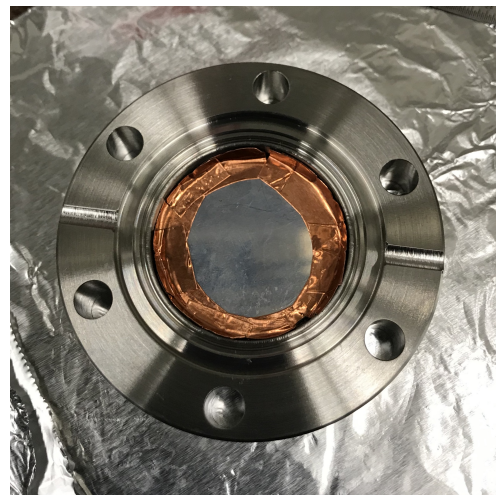


Figure 1.30: Aluminum coated plastic scintillator grounded by steel flange via conductive tape.

To see the beam a new detector was built out of a photo-multiplier tube (PMT) and a plastic scintil-

lator to replace the silicon detector. The idea was to have an aluminum coated plastic scintillator with the coated side facing the beam and the plastic side facing the PMT. An important aspect was that the coated side be grounded via conductive tape to the steel flange surrounding the scintillator (see Fig. 1.30). This would prevent charge from building up like it did on the silicon detector.

To analyze our findings, the output signal from the PMT was taken by a spectroscopy amplifier and the interpreted by a multichannel analyzer (MCA). The MCA data would then be obtained through a software called MAESTRO. A spectroscopy of a cesium source as well as the background was taken and used to calibrate the channels of the histograms received by MAESTRO. Finally, the beam minus background spectroscopies were converted to text files and analyzed in Excel (see Fig. 1.31).

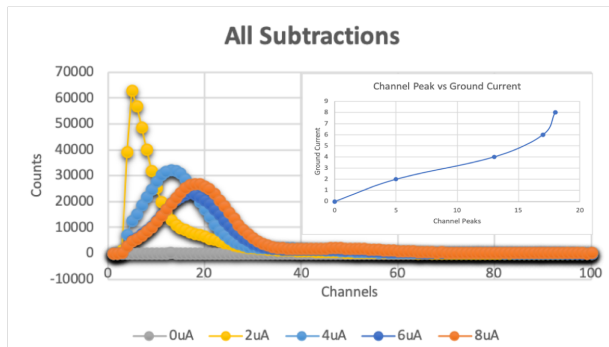


Figure 1.31: Channels versus Counts of different energies with the channel peaks plotted versus the ground current.

Investigation of the resistor chain showed charge loss around the middle. Between the reestablishment of a good resistor connection and the liquid nitrogen Dewar switch, the arcing and charge loss solutions were a total success. After the resistor chain fix, we purged the tent for a weekend. With just a weekend of consistent flow, the arcing ceased and the ground and terminal currents became consistent (see Fig. 1.32).

Lastly, the beam we saw consistent with the theory. The energy output was the expected value and the peak channels increased with the ground current value. The inductor voltage now determines the ground current, and the ground current determines the energy output of the beam.

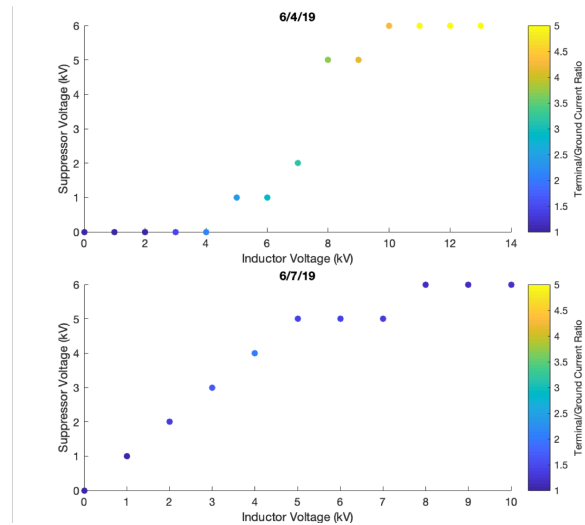
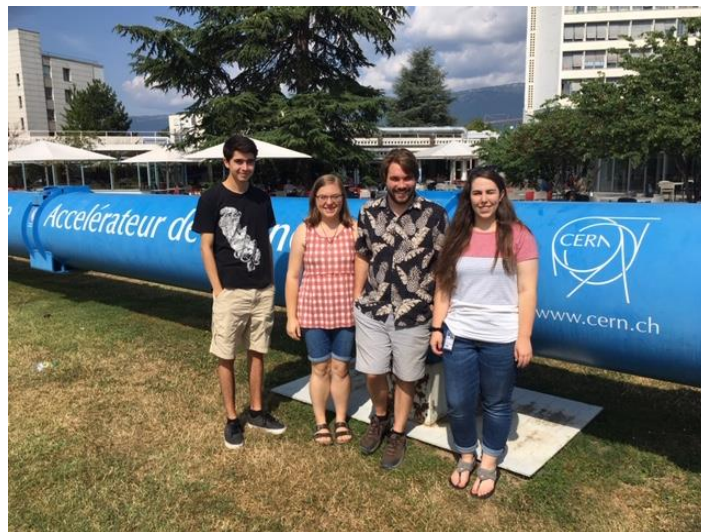


Figure 1.32: Improvement of ground and terminal current consistency after tank to Dewar switch

Research Based at CERN

Chapter 2



2.1 Studies of Top Quark Decay Kinematics

H. NELSON, *North Park University, Chicago, IL*; A. KOTWAL, K. PACHAL, *Duke University, Durham, NC*

If the Higgs Boson is made of new constituent particles, it is likely that the top quark is also made of similar particles based on how strongly they couple. In this case, events with four top quarks would be produced in excess of predictions from current theories. The purpose of this project is to study top quark kinematics to determine how to distinguish between background and signal top decays based on top quark transverse momentum. We used MADGRAPH to generate Monte Carlo events where t and \bar{t} decay to a bottom quark and a W boson, and the W bosons decay to $q\bar{q}$. Our analysis shows that as the top quark's transverse momentum increases, the distance between the top quark and its decays in the $\eta - \phi$ space decreases, where η is the pseudo-rapidity and ϕ is the azimuthal angle. This decrease in distance in the $\eta - \phi$ space as top transverse momentum increases demonstrates that the two high momentum tops in a four top process can be tagged primarily by using position.

Some Beyond the Standard Model (BSM) theories involve new heavy resonances that could couple preferentially with top or bottom quarks. If the heavy resonances only couple with the top or bottom quarks, they would have to be produced in a process like the one displayed in Fig. 2.1.

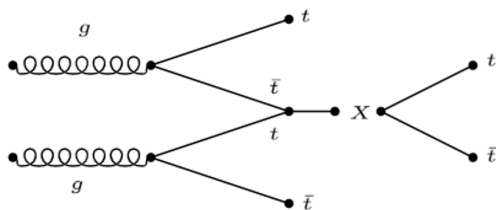


Figure 2.1: Proposed BSM process that creates four top quarks in the final state.

This process would create events where four top quarks would be produced in excess of predictions from current theories. If we find new heavy resonances that do have preferred coupling to the top, this could imply that the top quark is composite. Since this process would produce a final state with many top quarks, the kinematics of top quarks needs to be understood so that the four top process can be analyzed.

The process that produces four top quarks produces two top quarks with high momentum and two top quarks with low momentum. Top quarks always decay into a W boson and a bottom quark, regardless of how they are produced. This means that the kinematics of top quarks can be studied without producing the process that we will eventually search for. For this project, the top quarks with high momentum were studied, by looking at a process that creates two top quarks with high momentum. The studied process is shown in Fig. 2.2 where $t\bar{t}$ decays into W^+b and W^-b , and then the W^+ and W^- each decay into $q\bar{q}$. The goal of this project was to study how the transverse momentum of the top quark affects the distance between the parent top quark and its daughter decays.

Transverse momentum (p_T) is defined as the momentum in the xy plane because it is transverse to the beamline, which is defined as the z -axis. So, $p_T = \sqrt{p_x^2 + p_y^2}$. The angle between p_T and the x -axis is defined as ϕ . The angle between the three-vector momentum and the z -axis is defined as θ . From θ , the pseudo-rapidity is calculated as $\eta = \ln(\tan(\frac{\theta}{2}))$. An $\eta\phi$ space is created where $\Delta R = \sqrt{\Delta\eta^2 + \Delta\phi^2}$. Physically, ΔR can be thought of as the angular distance between two particles.

A data set of the process in Fig. 2.2 with 100,000 events was produced using MADGRAPH, a Monte Carlo simulation software package. MADGRAPH

simulated $p\bar{p} \rightarrow t\bar{t}$, $t \rightarrow W^+b$, $\bar{t} \rightarrow W^- \bar{b}$, $W^+ \rightarrow q\bar{q}$, and $W^- \rightarrow q\bar{q}$.

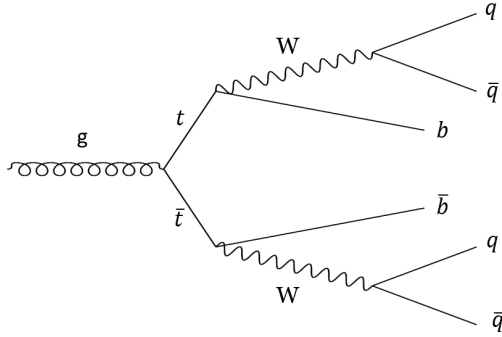


Figure 2.2: Feynman Diagram of $t\bar{t}$ decay.

First, I calculated η and ϕ for each bottom quark, W boson, and top quark parent. After pairing each bottom quark and W boson with its respective top quark parent, I calculated $\Delta\eta$ and $\Delta\phi$ for each bottom quark and W boson. $\Delta\eta = \eta_b - \eta_t$ or $\Delta\eta = \eta_W - \eta_t$ where t is the top quark parent to either the bottom quark or the W boson. $\Delta\phi$ was calculated using the ROOT Function, "DeltaPhi", to adjust for the fact that 0 and 2π are the same value. This ROOT function converts the $\Delta\phi$ value to be between $-\pi$ and π . Using $\Delta\eta$ and $\Delta\phi$, I calculated $\Delta R = \sqrt{\Delta\eta^2 + \Delta\phi^2}$ as seen in Fig. 2.3. This value is essentially the distance between the bottom quark or the W boson and its top quark parent.

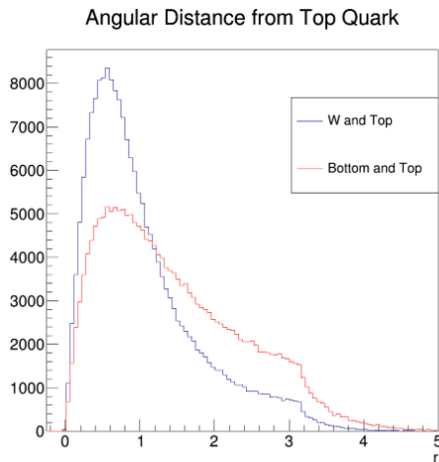


Figure 2.3: ΔR for the W boson and bottom quarks.

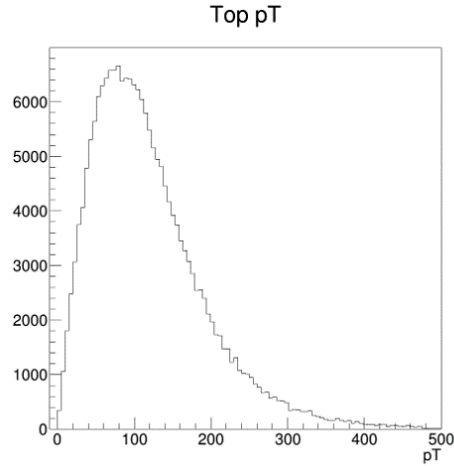


Figure 2.4: Top quark p_T .

Next, I plotted p_T for all of the top quarks (Fig. 2.4). I wanted to study how different ranges of top quark p_T effects the ΔR value. So, I separated top quark p_T into $p_T < 100$, $100 < p_T < 200$, $p_T > 200$ and calculated $\Delta\eta$, $\Delta\phi$, and ΔR for the three ranges of p_T for both each W boson and its top quark parent, and each bottom quark and its top quark parent. As top quark p_T increases, $\Delta\eta$ and $\Delta\phi$ are closer to 0. Also, as top p_T increases, the peak for $\Delta\eta$ and $\Delta\phi$ narrows. I then calculated ΔR for the W boson and the bottom quark with respect to its top quark parent, as shown in Figs. 2.5 and 2.6.

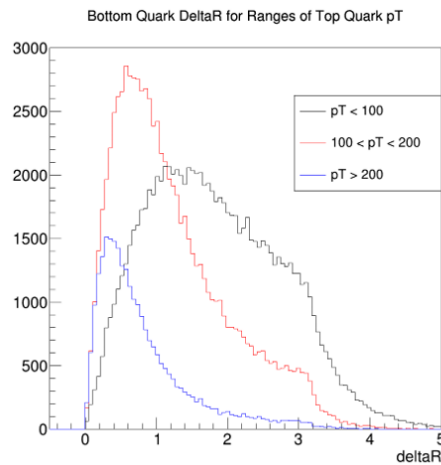


Figure 2.5: ΔR between bottom quarks and top quark parent for ranges of top quark p_T

In conclusion, as top quark p_T increases, ΔR for

the W boson and the bottom quark decreases. This means that as top quark transverse momentum increases, the distance that between the top quark decay products and its parent top quark decreases. Experimentally, this means that looking for top quarks with high momentum can primarily be done through position since the decays that will be detected are physically close to their parent particle in the detector.

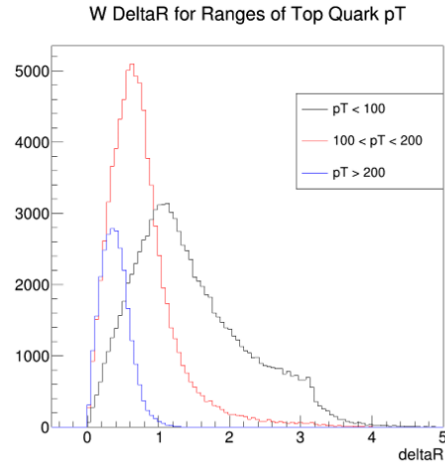


Figure 2.6: ΔR between W boson and top quark parent for ranges of top quark p_T

2.2 Tagging $c\bar{c}$ Events via Hadronic Decay Modes of J/ψ at ATLAS

S. CASTELLS, *University of Illinois, Urbana, IL*; N. DE GROOT, *Radboud University, Nijmegen, The Netherlands*

Searches for $c\bar{c}$ from Higgs/Z decays have been done exclusively for the ground J/ψ state using leptonic decay modes. This project aims to tag excited $c\bar{c}$ states via hadronic decay modes. The study of $c\bar{c}$ is relevant to Higgs coupling with the charm quark. Excited energy states such as $\psi(2S)$ and $\chi_{c0,c1,c2}$ are of interest as we can follow their decays into $J/\psi\gamma$. Excited states of $c\bar{c}$ are produced via the standard Higgs/Z production chain $gg \rightarrow H$ which creates $c\bar{c}$ by $H \rightarrow c\bar{c}\gamma$. The purpose of creating this tagging algorithm is to apply it to ATLAS data. The tagging is done using machine learning. Training data for the machine learning algorithm comes from Monte Carlo simulations of particle decays and simulations of interactions in ATLAS. Other Monte Carlo simulations are being tested to verify the stability of the algorithm. The accuracy for the fully-connected neural network trained on J/ψ , $\psi(2S)$, and quark/gluon background is 93%. This novel approach to $c\bar{c}$ tagging resulted in a production-ready tagger. Further study is being done using a convolution neural network for $c\bar{c}$ tagging.

Searches for charmonium, denoted by $c\bar{c}$, have exclusively been done for leptonic decay modes, of which e^-e^+ and $\mu^+\mu^-$ decays comprise a mere 6% each of the branching ratio for $c\bar{c}$ decays. Within those decay modes, tagging has only been done for the ground state of $c\bar{c}$, J/ψ . We study $c\bar{c}$ that is produced via the $H \rightarrow c\bar{c}\gamma$ process as shown in Fig. 2.7. As opposed to tagging $c\bar{c}$ through leptonic decay modes, we are tagging via its hadronic decay modes, which comprise the remaining 88% of the branching ratio. While this improves our ability to collect statistics, it also introduces issues that cannot be solved through traditional tagging methods. The 88% of the branching tree that includes the hadronic decay modes is comprised of a multitude of decay products which are difficult to tag due to their sheer number.

Our goal is to expand upon current tagging techniques to learn more about $c\bar{c}$. Knowing the production rate of $c\bar{c}$ would allow us to determine the strength of the charm quark's coupling to the Higgs. To do so, we use machine learning as our tool, via the use of TensorFlow and Keras, to create a tagging algorithm. Machine learning allows us to go beyond standard tagging techniques and to isolate complex signals from the background. This is especially important in our case as charmonium's hadronic decay modes generate complex signals that have to be distinguished from a complex quark-gluon background.

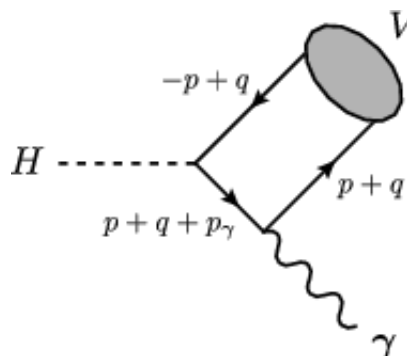


Figure 2.7: Feynman diagram showing the process which produces $c\bar{c}$ via Higgs decay. In this case, V represents the $c\bar{c}$ meson. The diagram shows the process in which a charm quark radiates a photon to then form the $c\bar{c}$ bound state. The opposite process where an anti-charm radiates a photon is merely a matter of swapping signs on the momentum.

Machine learning is emerging as a new and efficient way to tag particles within particle physics research. The idea behind machine learning is to train an algorithm to recognize patterns within data that may be difficult for humans to see and to get computers to learn based on examples. There are many different types of machine learning but the one rel-

evant to this project is fully-connected neural networks. This is the computer equivalent of neurons in one's brain but where each neuron is connected to every other neuron. There is some jargon used within machine learning that is useful to know: model is used interchangeably with algorithm; nodes can be thought of as neurons in a brain; layers are groups of nodes; descriptors are individual chunks of data; and activation functions are functions that enable nodes to pass along data. Papers going into further detail on these topics are cited when relevant throughout the report.

Fully-connected neural networks are called such because each node in one layer is connected to each node in the next layer. The architecture of a fully-connected neural network has an input layer, a number of hidden layers, and an output layer, where the input and output layers could have different dimensions. Hidden layers are called such because they are "hiding" in between the input and output layers and we cannot interact with them.

Now that the general notion of machine learning has been established, the focus shifts to dataset used to train and test the machine learning model. The data was simulated using Pythia and Delphes, emulating decays and interactions in the ATLAS detector. The simulations generated data on J/ψ , $\psi(2S)$, $\chi_{c0,c1,c2}$, and quark/gluon background, of which the mesons are in the ground state and various higher energy states of $c\bar{c}$, respectively. There are 16 variables within each descriptor and they are quite correlated individually. Each variable is either some observable quantity or directly calculable from observable quantities. A few of the variables were found to be irrelevant as they are completely correlated with other variables. The values of a couple of variables are plotted versus the confidence level from the algorithm as seen in Fig. 2.8. This figure shows that the algorithm is reasonably successful at distinguishing signal from background as seen by the high density of red and blue on their respective ends of the plots.

The dataset was used as input for the model to train on. The training and testing datasets do not necessarily have to be the same but during the development phase they were. Even with a decent input dataset, a model is only as good as its architecture enables it to be. The structure of the model consists of 16, 10, 9, 6, and 1 nodes in the 5 layers. The layers had corresponding activation functions of ReLU [Ram17] or tanh except for the output layer which had a sigmoid activation function. Dropout, a technique that turns off nodes at random in an attempt to

reduce over-training [Sri14], was used on each layer and varied between 0.1 and 0.35. The Adam optimizer [Kin14] was used with a learning rate of 0.03, which is relatively standard when using TensorFlow and Keras, and a binary cross-entropy loss function [Mil93].

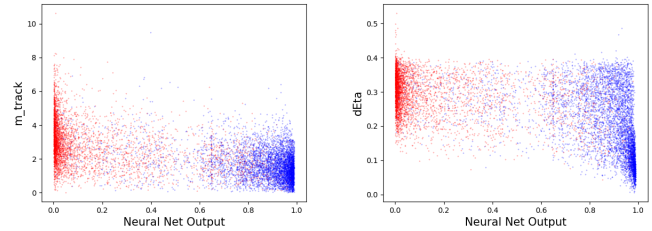


Figure 2.8: Plots of variable values versus confidence level. Values between zero and one indicate model confidence corresponding to background or signal, respectively.

The model has an accuracy of 93% when trained on a sample of J/ψ , $\psi(2S)$, $\chi_{c0,c1,c2}$, and quark/gluon background. We consider this to be a good level of accuracy to work with. In terms of performance among varying backgrounds, the model performs best with a purely gluon background while a purely quark background is harder to distinguish from signal. The final model performs on a mix of the two backgrounds and its accuracy is between what we would expect for this model when trained on either of the unmixed backgrounds individually.

After the success of a fully-connected neural network model, we have decided to expand into convolutional neural networks. We have generated "images" of $c\bar{c}$ decays and have run them through a basic convolutional neural network. The model currently over-trains so a larger data set is currently being simulated.

[Kin14] D. P. Kingma and J. Ba, arXiv preprint arXiv:1412.6980, (2014).

[Mil93] J. W. Miller, R. Goodman, and P. Smyth, IEEE Transactions on Information Theory, **39**, 1404 (1993).

[Ram17] P. Ramachandran, B. Zoph, and Q. V. Le, CoRR, **abs/1710.05941** (2017).

[Sri14] N. Srivastava *et al.*, Journal of Machine Learning Research, **15**, 1929 (2014).

2.3 Photo-bombing the Trigger: A Study of the Potential of Pileup in ATLAS Analysis

E. LYNN, *Taylor University, Upland, IN*; A.T. ARCE, K. PACHAL, *Duke University, Durham, NC*

This project explored the possibility of using pileup events, the proton-proton collisions that are automatically stored as the background to triggered events, to search for those processes that may currently be missed. If such events could be utilized, it would provide a new zero-bias sample of data for use. In order to determine the viability of this approach it was necessary to study what information about the pileup is available for analysis, as well as to test commonly used analysis tools to see if they are biased towards triggered events. During this project, vertices, muons, jets, and missing energy of pileup events were examined using a $Z \rightarrow \mu^+ \mu^-$ Monte Carlo file. It was determined that, though certain tools are biased towards a triggered vertex and would require modification, pileup contains the necessary information required for basic analysis and holds promise for future study.

At the Large Hadron Collider much more data is generated every second than CERN could ever hope to store. In an effort to keep only data of interest, a complex trigger system has been constructed. This system looks for interesting signatures such as especially high transverse momentum or unexpected behavior, and keeps only those events that meet such a threshold. As a result, beyond-the-standard model processes that may help explain dark matter or the mechanism of electroweak symmetry breaking might be missed at the LHC if they do not produce interactions that meet the trigger requirements.

The motivation for this project originated from a paper by Nachman and Rubbo [Nac18], which introduces and motivates the idea of using pileup as a zero-bias sample of low-momentum data from a technical perspective. Since this concept has not yet been implemented, it is necessary to study the characteristics and availability of pileup information before a pileup-based analysis can take place. This sort of study includes checking to make sure that necessary variables and objects are accessible in pileup data, whether the values for pileup properties are reasonable, and whether common software analysis tools are biased against pileup. A big part of this evaluation involved analyzing information from pileup and triggered (often referred to as the "primary") vertices separately and comparing the results. In this project, we try to answer questions such as these for vertices,

muons, jets, and missing transverse energy (MET) using a $Z \rightarrow \mu^+ \mu^-$ Monte Carlo (MC) file.

The first step in this study was to determine whether the most basic information necessary for any sort of analysis is readily available from pileup events, including vertex position, impact parameters, tracks associated to vertices, and the transverse momentum (p_T) of those tracks. We determined that all of this information is in fact easily accessible and realistic for the pileup events, just as it is for the triggered ones. To provide some context for the following results, it is helpful to be aware of some of the base statistics of the data set that we were using. The most relevant information is that there was always 1 primary vertex and a mean of 20 pileup vertices per event, there was a mean of 39 tracks per triggered vertex and 18 tracks per pileup vertex, and the sum p_T of the tracks from the triggered vertices had a mean of 99.7 GeV as opposed to 7 GeV for the pileup vertices. These findings are as expected, since the event that is triggered on is expected to be higher energy.

Once the basic information was deemed satisfactory, we began a slightly more complicated study of muons. At the same time we switched software frameworks from Analysis Base to Athena in order to more easily use certain analysis tools. Before studying muons in pileup we first had to implement a muon selection tool in order to work solely with muons that pass a medium quality cut as defined by the ATLAS

community based upon several muon characteristics. As expected for a $Z \rightarrow \mu^+ \mu^-$ MC file, events contained an average of 2 muons that passed the quality cut. Once we had effectively made quality cuts on the muons, we performed a simple resonance analysis on this file to further test the basic analysis capabilities. Fig. 2.9 presents the results of the resonance search in the pileup. Though hardly any pileup vertices meet the resonance requirements (as expected for a MC file), the few that do illustrate the promise and possibility for pileup analysis of this nature.

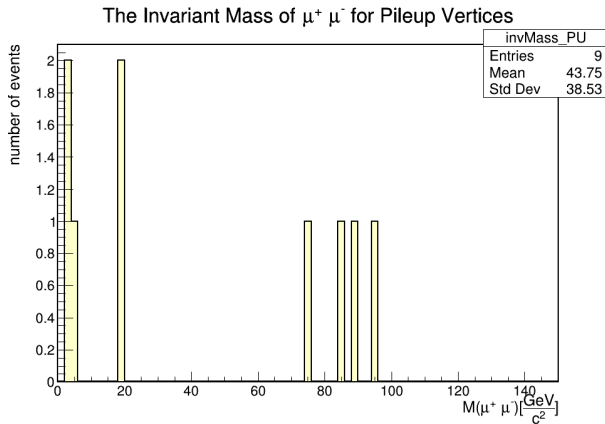


Figure 2.9: Invariant mass of a μ^+ and μ^- originating from a single pileup vertex.

After studying muons, we began to analyze jets. Normally the process of assigning jets to vertices would be accomplished using a software tool such as the Jet Vertex Tagger (JVT). However, after looking over the JVT code we discovered that it is only written for implementation with the triggered vertex and does not present an easy method for supplying an alternative input vertex. Therefore we devised our own method for assigning jets to vertices using the Jet Vertex Fraction (JVF) of each jet, which is a catalog of the fraction of tracks in a jet that originate from the possible vertices (including the pileup). This method required a different MC file however, since the original one did not contain the JVF vector for the jets. Our method was to assign a jet to a vertex if the JVF for that vertex was at or above 60%. In the case in which no vertex has a JVF value of 60% or more for the given jet, we labeled it as a stochastic jet (one likely composed of random overlapping tracks instead of a real jet originating from a single vertex). Fig. 2.10 shows the number of jets assigned to pileup vertices per event. Even though there are far more pileup vertices than triggered ones, the number of as-

signed jets are very similar, indicating that far more jets originate from triggered vertices (as expected). In addition, we obtained an average of 11 stochastic jets per event.

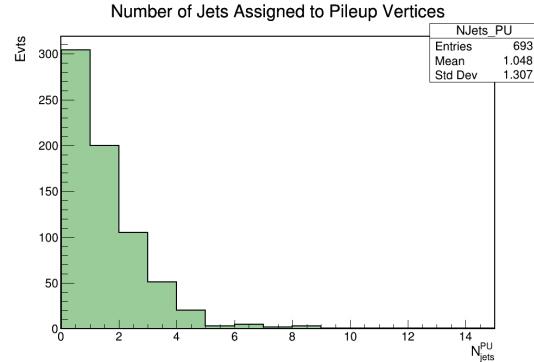


Figure 2.10: Number of pileup jets per event. This analysis only includes jets with a p_T above 17 GeV, since below that threshold ATLAS cannot calibrate jets.

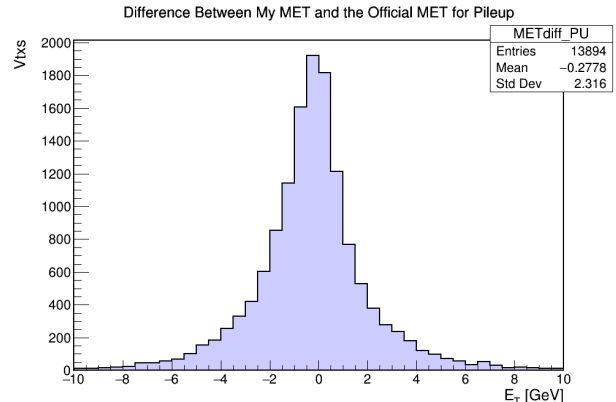


Figure 2.11: Difference between the two methods of calculating a track-based MET. A difference of a couple of GeV is to be expected considering the difference in levels of sophistication between the methods.

Finally we studied missing transverse energy (MET) in the pileup. Specifically, we wanted to use a track-based MET because when we use tracks we can reliably assign energy deposits to a particular vertex, whereas when we use calorimeter clusters it is harder to pinpoint where they come from. Our main goal for this study was to determine whether the official track MET for the pileup vertices is realistic. Towards that end we performed a quick and basic vector calculation of missing energy using the p_T of all of the tracks originating from each vertex, then

calculated the difference between our quick method and the official track MET. As seen in Fig. 2.11, the difference between the two methods is mostly lower than 2 or 3 GeV, which we consider an indication that the official MET is in fact reasonable and usable.

Overall, we found that pileup data shows great promise as a zero-bias sample for use in analysis, as we have concluded that the basics elements of vertices, muons, jets, and MET are readily available and reasonable. To best allow for effective usage, however,

future work will have to be done to study other objects in pileup, as well as to adjust useful tools such as the JVT to allow implementation with pileup objects.

The code for this project can be found in the repository: <https://gitlab.cern.ch/atlas-inst-duke-jetsrus/anapu>

[Nac18] B. Nachman and F. Rubbo, arXiv:1608.06299 [hep-ph], (2018).

2.4 Estimating the Background of Dark-QCD Processes

D. ROCHA, *Harvey Mudd College, Claremont, CA*; J. BEACHAM, *Duke University, Durham, NC*

We report our findings for a data-driven approach to estimating the background of Hidden Valley processes, which could lead to the discovery of a dark sector and a possible explanation for dark matter. The implementation and modification of an ABCD method is detailed and tests of the method upon background simulation are presented.

There are countless possibilities for what could be the true nature of dark matter, but one possibility is a so-called “Hidden Valley”, or “**dark sector**”. There’s no particular reason why dark matter should only be one species of matter. One could easily imagine a family of dark particles which rarely interact with normal matter. After all, Standard Model (SM) particles seem to follow patterns where particles form pairs and triplets with shared properties. We consider the possibility that there might be dark force carriers, dark leptons, and even dark composite particles. If the dark sector is a reality, then collisions at ATLAS could be producing many dark particles which escape our detection because of their long lifetimes and weak interactions with normal matter. In particular, a *dark pion*, a dark composite particle similar to that of the SM pion, could leave an interesting fingerprint in the detectors. For a while, this dark pion would travel undetected, but then it would decay into SM particles. Normally tracks left in the detectors of ATLAS are traced back to the center of the detector, and are reconstructed into *primary vertices*, which are where the proton-proton collisions happen. Because the dark pion has a macroscopic lifetime, its signature would be a *displaced/secondary vertex*. In most cases, displaced vertices are assumed to be track reconstruction errors, decays from particles originating outside of ATLAS, or interactions between the produced particles and the detectors. However, in the scenario where dark pions are produced in ATLAS, these displaced vertices could hold the key to observing the dark pion and declaring a discovery.

While calculating the signal characteristics of dark sector processes is an increasingly well-studied area of research, determining the SM background proves more difficult. Hadronization is a complicated,

nonlinear process, and theoretical calculations don’t always yield the most accurate results. To accurately estimate the background of dark sector processes, we implement a data-driven approach: the ABCD method. We chose the ABCD method because it does not rely at all on simulated events. It is an extrapolation technique that is applied directly to data.

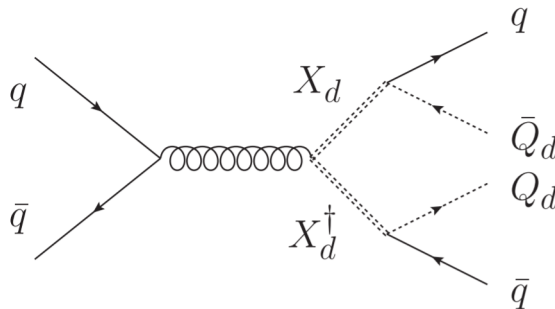


Figure 2.12: Feynman diagram for the production of two dark jets (Q_d) and two SM jets, via two dark force carriers (X_d).

The specific process we consider is the production of two dark quarks (Q_d) and two SM quarks via two dark force carriers (X_d), shown in Fig. 2.12. The two SM quarks then hadronize into standard jets, and the two dark quarks hadronize into dark jets. We assume that when these dark quarks hadronize, some of them become dark pions, and some of the dark pions decay within the detectors. This dark jet, which appears to the trigger as a normal jet at first, will contain a bunch of displaced vertices. Jets with multiple secondary vertices inside them are known as *emerging jets* (see Fig. 2.13). Emerging jets can be produced by a number of different theorized interactions, but

we consider the case where dark pions produce the displaced vertices within an emerging jet.

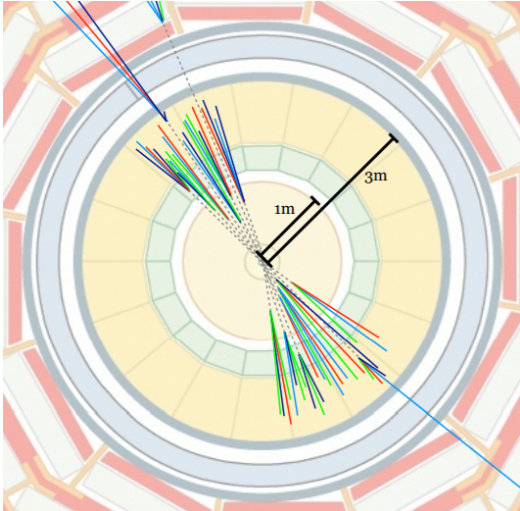


Figure 2.13: A diagram of two emerging jets produced in ATLAS. (Borrowed from Schwaller et al. [Sch15].)

The ABCD method is an alternative method of searching for a signal. Instead of attempting to tag a single jet correctly as an emerging jet, the ABCD method uses event-level variables to separate the signal from background. We therefore require measurement variables which provide signal-background separation. An obvious variable choice is the number of secondary vertices in an event; this number is expected to be much higher for dark sector events than for standard events. Another variable is the total jet transverse momentum (P_T) for the four jets with the highest P_T . We expect this to be much higher for dark sector processes, because the dark force carrier is very heavy and will carry away a lot of energy and momentum from the collision point. These two variables provide enough separation to apply the ABCD method.

We also define a search region and validation region within the parameter space. We expect the dark sector signal to be present only in events with four jets, so we define a *search region* that contains events with four jets with $P_T > 50$ GeV. However, we would like to be able to test our methods on data that does not contain signal, so we define a *validation region* to contain events that have either two or three jets with $P_T > 50$ GeV. While we are testing our methods, we would like to be blind to the signal, so we can use the simulation in either search or validation regions, but

we may only use data in the validation region. Later, when we finalize the analysis, the data in the search region may be used.

The ABCD method is a fairly simple process; though we have expanded upon the basic idea to refine the accuracy. An extensive outline can be found online in the CERN twiki [But18]. The basic idea is as follows.

1. Plot signal and background on 2D-plane. Make sure there is ample separation, and very little correlation in the background variables.
2. Divide the plane into 4 quadrants such that the signal is contained in only one quadrant. Label this region A.
3. Use a ratio equation to extrapolate an expectation value for region A.

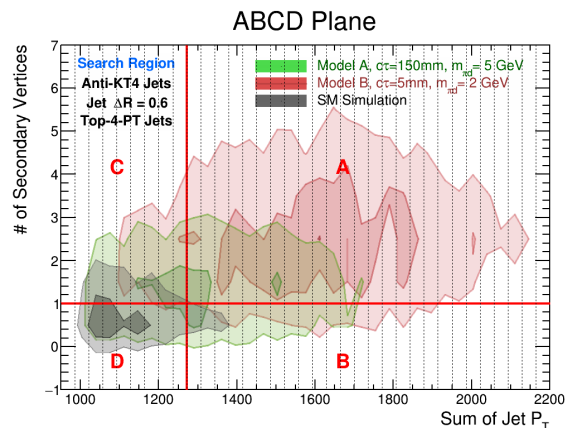


Figure 2.14: ABCD method regions for two different dark-QCD models. The red lines represent the region boundaries, and the dotted lines are the regions that have been sliced into strips, which is used in the second method.

For the variables previously described, the signal-background separation is sufficient (see Fig. 2.14). The signal for Model A is concentrated more towards region A than the background, which would allow us to detect a signal. For Model B, there is much better separation, which suggests that ATLAS would be most sensitive to this set of parameters. Because the variables used in the ABCD plane are uncorrelated, the y-distribution must *look* the same anywhere along the x axis. Thus, the ratio

$$\frac{N_C}{N_D} = \frac{N_A}{N_B} \quad (2.1)$$

must hold. In a perfect world, this would predict the number of background events in the region A, and one could determine if an excess of events is seen in the data. One could propagate errors and calculate uncertainty on this value. However, if the variables have even a slight correlation, this prediction would be skewed significantly. It is for this reason that we decided to adjust our technique. Instead of using a simple fraction, we used a more complicated method. The new method is as follows.

1. Set up 2D plane same as the initial method.
2. This time, cut the regions C and D into strips along the y axis (see Fig. 2.14). Then, for each of these strips, calculate the value

$$r_i = \frac{N_{C,i}}{N_{D,i}} \quad (2.2)$$

where i is the index of the i th strip.

3. Fit a line to the ratios r_i .
4. Cut the region B into strips along the y-axis, in the same manner as done with D and C.
5. Using the fit, extrapolate the ratio and the error on the ratio for each strip in B.
6. Using the extrapolated values and the number of events in each strip, calculate a value for the total events found in region A.

This method is more flexible, but in some cases, it is more vulnerable. Extrapolating along the x-axis using only a handful of data points can lead to disastrous results. This happens when we run this version of the ABCD method on the background distribution in the signal region (4 jets with $P_T > 100$ GeV), shown in in Fig. 2.14. It is fooled by the spread of points at the beginning, as there is an apparent downward trend that does not continue past the region C/D cutoff (see Fig. 2.15a). This, of course, would be catastrophic to the search, because it would lead to a false declaration of discovery!

On the other hand, there are instances where the fitting method works well. If we instead switch from

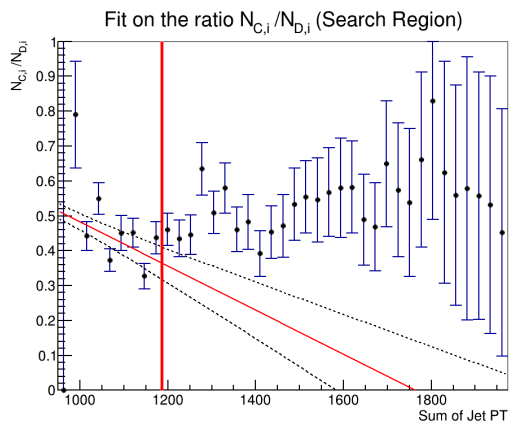
the signal to the validation region, we let in many more points, and the error bars tighten a lot. In this case, the fit nails both the expected value and the spread! We expect to have a lot of points in our data set, so we chose to move forward with the fitting method.

To deal with the potentially catastrophic fitting mistake, we introduced what will be called a “confirmation region”. That is, we would single out the next couple points on the plot and test the fit, to see if it gets reasonable results. In the first plot, we would successfully recognize that the fit was not accurate and not be tempted to declare a discovery. In fact, on the exact example above, choosing the next four ratio points as a confirmation region, we discover that the predicted value of the confirmation region is 312 ± 46 , but the true value is 452 ± 21 , which is a difference of 2.8 standard deviations. If we saw something like this, we would have to question whether the fit was working. Using the confirmation region could be a useful tool for analyzing our data with a careful eye.

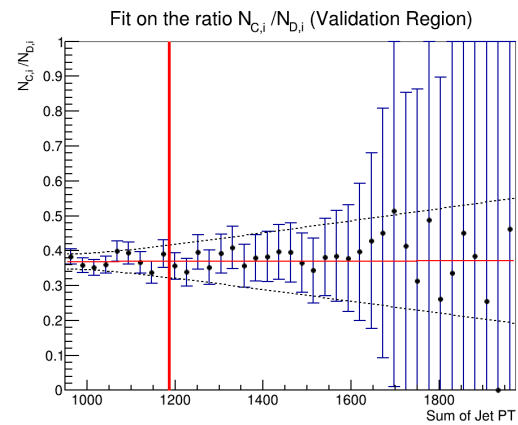
Dark matter could be hiding in the most unexpected of corners. In this analysis we have chosen a very specific place that dark matter might be found, namely, in emerging jets. The ABCD method allows us to investigate emerging jets by analyzing collision data, and not worry about rough-around-the-edges SM calculations. In the future, we plan to continue this analysis and estimate the sensitivity of ATLAS given various dark sector parameters. This will allow us to quantify how much of the dark sector parameter space that we can cover. Additionally, we hope to increase the accuracy and quantity of dark sector simulated events and find variables that will give ideal signal-background separation in the ABCD plane.

[But18] W. Buttinger, “*Background Estimation with the ABCD Method*”, 2018, <https://twiki.cern.ch/twiki/bin/view/Main/ABCDMethod>.

[Sch15] P. Schwaller, D. Stolarski, and A. Weiler, JHEP, **arXiv:1502.05409** (2015).



- (a) For the background simulation in the search region, the fitting method fails. The estimated number of events in region A was calculated to be $N_A = 613 \pm 76$, and the true number was $N_A = 1281 \pm 36$.



- (b) For the background simulation in the validation region, the fitting method works. The estimated number of events in region A was calculated to be $N_A = 794 \pm 35$, and the true number was $N_A = 801 \pm 28$.

Figure 2.15: Examples of how the fitting method works on different slices of the simulation.





Index

Aneke, E., 20

Bradford, R.W., 15

Castells, S., 27

Contreras, B., 4

Lynn, E., 29

McEneaney, M., 6

Meyer, T., 12

Nelson, H., 24

Richards, T., 2

Rocha, D., 32

Smith, E., 17

Wolsey, K., 9